Flux Linkage-Based Direct Model Predictive Current Control for Synchronous Machines

Sebastian Wendel, *Graduate Student Member, IEEE*, Petros Karamanakos, *Senior Member, IEEE*, Philipp Gebhardt, Armin Dietz, and Ralph Kennel, *Senior Member, IEEE*

***Abstract*—This article presents a flux linkage-based direct model predictive current control approach that achieves favorable performance both during steady-state and transient operation. The former is achieved by computing the optimal time instants at which a new switch position is applied to the converter. To this end, the future current behavior is not computed based on the machine inductances or inductance look-up tables; instead, flux linkage maps are utilized to predict the trajectory of the magnetic flux linkage, and subsequently of the current. This is advantageous for electric drives with noticeable magnetic nonlinearity in terms of saturation and/or cross-coupling effects. Hence, by using flux linkage maps in the prediction process, the evolution of the stator current can be calculated more accurately, enabling the controller to make better switching decisions. Moreover, the discussed predictive controller exhibits excellent dynamic performance owing to its direct control nature, i.e., the control and modulation tasks are performed in one computational stage rendering a dedicated modulation stage redundant. Three different drive systems based on permanent magnet synchronous motors are examined to demonstrate the effectiveness of the presented control approach.**

***Index Terms*—AC drives, direct control, finite control set MPC (FCS-MPC), flux linkage maps, implicit modulator, model predictive control (MPC), SoC FPGA, synchronous machines.**

I. Introduction

FINITE control set model predictive control (FCS-MPC), also known as direct model predictive control (DMPC), computes the constrained optimal switch position based on a predefined cost function, and, subsequently, it directly applies it to the power converter. By doing so, the control objectives, such as output reference tracking and minimization of the switching frequency, are met, while very fast transient responses are achieved due to the direct control principle of DMPC. Moreover, when long prediction horizons are implemented, the closed-loop stability margin is improved [1]. The same applies to the system performance, as highlighted by the reduced total harmonic distortion (THD) of the variables of concern for a given average switching frequency f_{sw} [2].

Nowadays, readily available powerful control platforms, such as system-on-a-chip field-programmable gate arrays (SoC FPGAs), facilitate the real-time implementation of long-horizon DMPC with control frequencies f_{cf} up to several hundred kHz [3]. However, in power electronic systems with time constants of just a few ms—or even μs—such as small electric drives, the granularity of switching may still be too low for an acceptable torque and current ripple. In particular, as reported in [4, Section V], the control frequency should be about two orders of magnitude higher than the average switching frequency for a favorable performance.

As can be understood, a combination of high switching granularity, as realized, e.g., with carrier-based pulsewidth modulation (CB-PWM) or space vector modulation (SVM), and fast dynamic response of DMPC seems beneficial. Therefore, introducing the concept of variable switching points (VSPs), i.e., time instants within the control interval T_{cf} at which the converter switches change state (also referred to as switching instants), to the DMPC problem is meaningful. In doing so, DMPC can apply more than one switch position to the converter within one T_{cf}. Thus, higher switching granularity can be achieved, which, in turn, allows for a reduction of the current and torque distortions. Motivated by this, several works have adopted the notion of VSP and combined it with DMPC, see, e.g., [5]–[18]. Owing to the introduced VSPs, these approaches can implement up to four different switch positions in one control interval T_{cf}. For example, MPC-based methods, such as in [15], decide on whether to apply one or two new switch positions within one T_{cf}, in [6] and [9] two different switch positions are implemented, whereas four different switch positions (akin to SVM) are implemented in [12]–[14], [18].

All previous approaches, when designed for electrical drives, see, e.g., [5]–[7], [10], [13]–[15], use prediction models that rely on knowledge of the (absolute) motor inductances for computing the optimal switch positions and the corresponding VSPs. This might be accurate enough for drives based on induction motors or permanent magnet synchronous motors (PMSMs) with surface mounted magnets (SPMSMs) operating in the linear region of the magnetic circuit. However, when machines with a

Manuscript received December 26, 2020; revised March 27, 2021; accepted May 15, 2021. Date of publication May 25, 2021; date of current version August 16, 2021. This work was supported by the Bavarian Ministry of Economic Affairs, Energy and Technology under Grant ESB048/004. Recommended for publication by Associate Editor L. V. Iyer. *(Corresponding author: Sebastian Wendel.)*

Sebastian Wendel, Philipp Gebhardt, and Armin Dietz are with the Institute ELSYS, Technische Hochschule Nürnberg, 90489 Nuremberg, Germany (e-mail: sebastian.wendel@th-nuernberg.de; gebhardtph60189@th-nuernberg.de; armin.dietz@th-nuernberg.de).

Petros Karamanakos is with the Faculty of Information Technology and Communication Sciences, Tampere University, 33101 Tampere, Finland (e-mail: p.karamanakos@ieee.org).

Ralph Kennel is with the Chair of Electrical Drive Systems and Power Electronics, Technical University Munich, 80333 Munich, Germany (e-mail: ralph.kennel@tum.de).

Color versions of one or more figures in this article are available at https://doi.org/10.1109/TPEL.2021.3083657.

Digital Object Identifier 10.1109/TPEL.2021.3083657

strong nonlinear magnetic circuit are of concern, such as interior PMSMs (IPMSMs), the prediction model accuracy degrades. Especially when considering highly utilized IPMSMs, which are getting more and more popular due to the associated reduced manufacturing cost and weight, it is evident that an accurate prediction model is crucial since saturation effects appear already in the nominal range [19]. Such a need becomes even more prominent given that cross-coupling effects are almost always present and cannot be neglected for most IPMSM designs [20].

In case of conventional DMPC, there are several approaches that address the adverse impact of an inaccurate inductance on the controller performance; see, e.g., [21]–[25]. For instance, a cost function is proposed in [22] where an integral term of the current-tracking error is added to equip the control scheme with an element of integrating nature. The associated control gains, however, are tuned heuristically, implying that optimal performance for the whole operating regime is not ensured. Zhang *et al.* [23] superimpose an observer, but due to the convergence of the algorithm—which requires several fundamental periods—it is not suitable for dynamic processes. In [24] and [25], model-free—also called nonparametric—MPC is used to tackle potential model mismatches. In principle, these model-free approaches are based on the difference between the last measured and previously predicted current. Moreover, they have to be averaged over several samples to avoid a negative influence of measurement outliers. Thus, parameters that are initially determined inaccurately or are slowly varying, e.g., due to temperature drifts, can be compensated for very well. However, in case of, e.g., an increasing current reference, a significant degree of saturation can be reached within a few control steps. If this event is to be covered, i.e., predicted over the horizon, the knowledge of previous control steps does not provide any valuable information. As a result, an accurate prediction of the system state becomes challenging since saturation can cause a highly nonlinear behavior. Hence, based on the above, it can be claimed that for a dynamic, accurate prediction, a different approach needs to be devised that will enable accurate predictions both during transients and in steady state, shortly after a transient.

To address the aforementioned issue, some works aim to increase the modeling accuracy instead of correcting simple models by adding averaged model deviations from the past. For example, Štumberger *et al.* [20] proposed the use of differential inductances L_{dd}, L_{dq}, L_{qq}, and L_{qd}. Using the latter for the prediction model of DMPC, however, introduces four three-dimensional maps, which implies higher memory requirements for storing them, which ensues increased computational effort for traversing and using them. Moreover, due to their dependency on the changes in the current, they are susceptible to noise-contaminated current measurements, as explained later in the article.

Motivated by the above, the novelty of this article relates to the design of an MPC algorithm—named variable switching point predictive current control (VSP^{2}CC)—that employs the notion of VSPs and bases the prediction process on flux linkage maps. In doing so, the developed control method is intuitively accessible since the flux linkage directly describes the machine behavior.

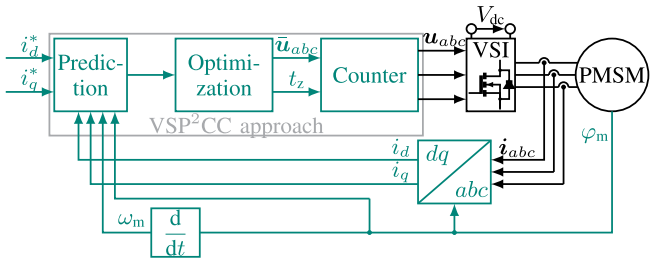

Fig. 1. VSP^{2}CC with current reference tracking for a two-level VSI with a PMSM.

Moreover, it comes with modest computational requirements as only two maps are required, in contrast to the four maps required for an inductance-based prediction model. Thanks to the above, the proposed VSP^{2}CC algorithm can accurately predict the future stator current behavior even for magnetically nonlinear IPMSM drives over the entire operating range. This enables the calculation of more effective VSPs, which means that the proposed VSP^{2}CC method can achieve favorable steady-state system performance—quantified by the stator current THD—as well as very fast dynamic responses, limited only by the available dc-link voltage. Moreover, by employing a simple but inherent online flux linkage map identification, the proposed MPC algorithm becomes more robust to system parameter variations since it adjusts the flux linkage maps during operation. Thus, it does not require detailed prior knowledge of the machine inductances.

The rest of this article is structured as follows. Section II introduces the drive system and the proposed prediction model. Section III presents an identification method which adapts the flux linkage of the PMSM in a time-uncritical task during operation. The proposed flux linkage-based direct MPC algorithm is presented in Section IV, while its resource-efficient implementation on an FPGA is provided in Section V. The performance of the introduced control method is assessed in Section VI for three different drive systems. Finally, Section VII concludes the article.

II. Control Model

The proposed flux linkage-based VSP^{2}CC approach is developed for drives that consist of a three-phase two-level voltage source inverter (VSI) and either an SPMSM or an IPMSM; see Fig. 1.

The modeling of the drive system is performed in the dq-plane, i.e., a two-dimensional reference plane which rotates with the electrical angular speed ω_{el}. With the knowledge of the rotor flux angle φ, the matrix

$$\boldsymbol{K}(\varphi) = \frac{2}{3}\begin{bmatrix} \cos(\varphi) & \cos\left(\varphi - \frac{2\pi}{3}\right) & \cos\left(\varphi + \frac{2\pi}{3}\right) \\ -\sin(\varphi) & -\sin\left(\varphi - \frac{2\pi}{3}\right) & -\sin\left(\varphi + \frac{2\pi}{3}\right) \end{bmatrix}$$

is used to transform any three-phase variable $\boldsymbol{\xi}_{abc} = [\xi_a\, \xi_b\, \xi_c]^T$ into a two-dimensional variable $\boldsymbol{\xi}_{dq} = [\xi_d\, \xi_q]^T$ through the operation

$$\boldsymbol{\xi}_{dq} = \boldsymbol{K}(\varphi)\boldsymbol{\xi}_{abc}. \tag{1}$$

Note that, as indicated in Fig. 1, the mechanical rotor position φ_{m} is measured, and used to compute the mechanical angular speed ω_{m}. The latter relates to the electrical angular speed with $\omega_{\mathrm{el}} = p\omega_{\mathrm{m}}$, where p is the number of pole pairs.

A. Nonlinear Model of the Drive System

The drive system is controlled by directly manipulating the switches of the VSI. Given that the single-phase switch position assumes values $u_x \in \{-1, 1\}$, with $x \in \{\mathrm{a}, \mathrm{b}, \mathrm{c}\}$, the output of the inverter in the dq-plane is

$$\boldsymbol{v}_{dq,\mathrm{inv}} = \frac{V_{\mathrm{dc}}}{2}\boldsymbol{K}(\varphi)\boldsymbol{u}_{abc} \tag{2}$$

where $\boldsymbol{u}_{abc} \in \{-1, 1\}^3$ is the three-phase switch position and V_{dc} the dc-link voltage. Note that the $2^3 = 8$ possible switch positions result in seven unique voltage space vectors (SVs). Specifically, two of the switch positions, i.e., $\boldsymbol{u}_{abc} = [111]^T$ and $\boldsymbol{u}_{abc} = [-1-1-1]^T$, short-circuit the load, and thus they correspond to two SVs, named zero SVs, that are redundant. The remaining combinations lead to unique SVs called active SVs. As can be seen in Fig. 1, the VSI output voltage $\boldsymbol{v}_{abc,\mathrm{inv}}$ is equal to the stator voltage $\boldsymbol{v}_{abc}$, i.e., $\boldsymbol{v}_{abc,\mathrm{inv}} = \boldsymbol{v}_{abc} = \frac{V_{\mathrm{dc}}}{2}\boldsymbol{u}_{abc}$ in the abc-plane. Hence, according to (2), it holds that $\boldsymbol{v}_{dq,\mathrm{inv}} = \boldsymbol{v}_{dq}$, with $\boldsymbol{v}_{dq} = [v_d\ v_q]^T$ being the stator voltage in the dq-plane given by

$$\boldsymbol{v}_{dq}(t) = R_{\mathrm{ph}}(\vartheta)\boldsymbol{i}_{dq}(t) + \frac{\mathrm{d}\boldsymbol{\psi}_{dq}(t)}{\mathrm{d}t} + \omega_{\mathrm{el}}(t)\boldsymbol{Q}\boldsymbol{\psi}_{dq}(t) \tag{3}$$

where $\boldsymbol{i}_{dq} = [i_d\ i_q]^T$ is the stator current, and $\boldsymbol{\psi}_{dq} = [\psi_d\ \psi_q]^T$ is the flux linkage whose d-component is $\psi_d(t) = \psi_d^*(t) + \psi_{\mathrm{PM}}(\varphi, \vartheta_{\mathrm{m}})$, where ψ_{PM} is the permanent magnet flux constant. Note that the flux linkages on the d- and q-axis depend on the respective currents and the electrical rotor position φ, while the permanent magnet flux linkage ψ_{PM} varies with φ and the magnet temperature ϑ_{m}. Finally, R_{ph} is the stator resistance, and $\boldsymbol{Q} = \begin{bmatrix} 0 & -1 \\ 1 & 0 \end{bmatrix}$. It is worth mentioning that even if saturation and cross-coupling effects increase through the use of highly utilized synchronous machines, (3) includes these effects. For example, as shown in [20], [26, p. 20], the flux linkage change can be described by

$$\Delta\psi_d = \frac{\mathrm{d}\psi_d(t)}{\mathrm{d}t} = \underbrace{\frac{\partial\psi_d^*}{\partial i_d}}_{L_{dd}}\frac{\mathrm{d}i_d(t)}{\mathrm{d}t} + \underbrace{\frac{\partial\psi_d^*}{\partial i_q}}_{L_{dq}}\frac{\mathrm{d}i_q(t)}{\mathrm{d}t} + \underbrace{\frac{\partial\psi_d}{\partial\varphi}}_{\Lambda_d\approx 0}\underbrace{\frac{\mathrm{d}\varphi(t)}{\mathrm{d}t}}_{\omega_{\mathrm{el}}(t)} \tag{4a}$$

$$\Delta\psi_q = \frac{\mathrm{d}\psi_q(t)}{\mathrm{d}t} = \underbrace{\frac{\partial\psi_q}{\partial i_q}}_{L_{qq}}\frac{\mathrm{d}i_q(t)}{\mathrm{d}t} + \underbrace{\frac{\partial\psi_q}{\partial i_d}}_{L_{qd}}\frac{\mathrm{d}i_d(t)}{\mathrm{d}t} + \underbrace{\frac{\partial\psi_q}{\partial\varphi}}_{\Lambda_q\approx 0}\underbrace{\frac{\mathrm{d}\varphi(t)}{\mathrm{d}t}}_{\omega_{\mathrm{el}}(t)}. \tag{4b}$$

Respecting cross-coupling effects by using the flux linkage is in theory more accurate [27] since it avoids the calculation of derivatives required to derive the differential inductances L_{dd}, L_{dq}, L_{qq}, and L_{qd}. As can be deduced from (4), these inductances depend on the current changes, and hence their computation is susceptible to noise-contaminated current measurements. To avoid such adverse complications, an online identification of the flux linkage is adopted in this work; see Section III.

B. Inductance-Based Prediction Model

When MPC for PMSM-based drives is employed to control the stator current, the common practice is to compute the evolution of the latter based on the (time-varying) absolute inductances L_d and L_q [3]. Specifically, by applying forward Euler discretization to (3), and with the help of (4), the predicted current $\boldsymbol{i}_{dq}(k+1)$ is given by

$$\boldsymbol{i}_{dq}(k+1) = T_{\mathrm{cf}}\boldsymbol{L}^{-1}\Bigg(\boldsymbol{v}_{dq}(k) - R_{\mathrm{ph}}\boldsymbol{i}_{dq}(k) - \omega_{\mathrm{el}}(k)\Bigg(\boldsymbol{Q}\boldsymbol{L}\boldsymbol{i}_{dq}(k) + \begin{bmatrix} 0 \\ \psi_{\mathrm{PM}} \end{bmatrix}\Bigg)\Bigg) + \boldsymbol{i}_{dq}(k) \tag{5}$$

where T_{cf}[1] is the control interval and $\boldsymbol{L} = \mathrm{diag}(L_d, L_q)$. Hence, when constant inductances are assumed, (5) leads to less accurate predictions and, consequently, to potential performance deterioration.

C. Flux Linkage-Based Prediction Model

Using a flux linkage-based prediction model, the above mentioned issue can be addressed on the basis of (3). By employing again forward Euler discretization, the voltage equation (3) gives[2]

$$\boldsymbol{v}_{dq}(k) = R_{\mathrm{ph}}\boldsymbol{i}_{dq}(k) + \frac{\Delta\boldsymbol{\psi}_{dq}(k+1)}{T_{\mathrm{cf}}} + \frac{\omega_{\mathrm{el}}(k)}{2}\boldsymbol{Q}\Sigma\boldsymbol{\psi}_{dq}(k+1) \tag{6}$$

where $\Delta\boldsymbol{\psi}_{dq}(k+1) = \boldsymbol{\psi}_{dq}(k+1) - \boldsymbol{\psi}_{dq}(k)$ and $\Sigma\boldsymbol{\psi}_{dq}(k+1) = \boldsymbol{\psi}_{dq}(k) + \boldsymbol{\psi}_{dq}(k+1)$. Assuming a constant electrical speed ω_{el} and stator resistance R_{ph} during one control interval T_{cf}, and after some algebraic manipulations shown in the Appendix, the flux linkage at time step $k+1$ is given by

$$\boldsymbol{\psi}_{dq}(k+1) \approx T_{\mathrm{cf}}\frac{\boldsymbol{v}_{dq}(k) - R_{\mathrm{ph}}\boldsymbol{i}_{dq}(k) - \omega_{\mathrm{el}}(k)\boldsymbol{Q}\boldsymbol{\psi}_{dq}(k)}{1 + \frac{1}{4}T_{\mathrm{cf}}^2\omega_{\mathrm{el}}^2(k)} + \boldsymbol{\psi}_{dq}(k). \tag{7}$$

As can be seen, the above expression shows that the future behavior of the drive has been decoupled from the machine inductances, adding a high degree of robustness to variations in them. Finally, it should be mentioned that (7) is also used for the

[1]The interlock time (here 200 ns) is compensated for according to [28].

[2]To compensate for discretization errors introduced by the forward Euler method at high speeds, i.e., when $\omega_{\mathrm{el}}(\boldsymbol{\psi}_{dq}(k+1) - \boldsymbol{\psi}_{dq}(k)) \approx \boldsymbol{0}$ does not hold, using the average flux linkage over k and $k+1$ in (6)—instead of the flux at step k, i.e., $\boldsymbol{\psi}_{dq}(k)$—can improve the prediction accuracy; see [19]. For the speeds considered in the following, however, using the average flux does not offer any significant benefits compared to using $\boldsymbol{\psi}_{dq}(k)$.

compensation of the delay time, i.e., the time interval between the measurements occur and the execution of the control action, caused by the real-time system.

III. Flux Linkage Map Identification

The flux linkage can be described in two ways. First, analytically, by identifying a (high-order) polynomial function. With such an approach, self-saturation can be easily described, while bivariate polynomials can be used for the modeling of cross-saturation effects [29]. However, it is not trivial which polynomial order describes the nonlinearity satisfactory enough; a heuristic choice is to use a third to fifth-order polynomial [29], which may be computationally intractable in real time. Because of this as well as for implementation reasons (see Section V-B), a second method is preferred, which uses flux linkage maps. The identified three-dimensional flux linkage maps represent the value of the flux linkage components ψ_d and ψ_q as a function of the motor current components i_d and i_q. In this way, the maps provide information about linearity deviations including self- and cross-saturation.

There is a variety of approaches for online identification of the flux linkage maps; see, e.g., [26, p. 52], and [30]. However, the method proposed in this article uses an online flux linkage map identification, which enables the adaptation of the maps in a time-uncritical task during operation. The advantage of this method is its ease of implementation; it allows a simple and fast start-up by first using the linear parameters, i.e., the absolute inductances, while nonlinear effects are taken into account later in the process. It must be mentioned, however, that iron losses are not taken into account. Moreover, to avoid adding a fourth dimension in the generated maps—and thus keep the memory and computational requirements low—position-dependent changes (i.e., spatial harmonics) are neglected. As a result, the last term in (4) can be neglected, implying that a small prediction error is introduced. Such an error, however, can be regarded acceptable, especially when considering that winding effects, magnet arrangement, and manufacturing imperfections, which can lead to an unequal air gap—and thus an unequal air-gap field—are negligible within a small tolerance band [31].

A. Data Acquisition

The identification algorithm is initially based on the linear machine parameters R_{ph}, L_d, L_q, and ψ_{PM}, which describe the machine behavior sufficiently well for operation at low currents. With these parameters—which can be predetermined either by using an offline identification process or merely the datasheet values—the initial flux linkage $\boldsymbol{\psi}_{dq,\text{init}}$ is found by

$$\boldsymbol{\psi}_{dq,\text{init}} = \boldsymbol{L}\boldsymbol{i}_{dq} + \begin{bmatrix} \psi_{\text{PM}} \\ 0 \end{bmatrix}. \tag{8}$$

Subsequently, during operation, the flux linkage maps are adapted step by step to cover the nonlinear behavior of the magnetic circuit at higher currents. Due to the temperature dependency, R_{ph} must be identified online in regular intervals. Since the temperature-dependence coefficient of R_{ph} and ψ_{PM} can be determined offline in advance, it is possible to compensate for the temperature drift of both parameters during operation. In doing so, the algorithm is able to calculate the present flux linkage after rearrangement of (3), i.e.,

$$\boldsymbol{\psi}_{dq} = \boldsymbol{Q}^{-1}\frac{\boldsymbol{v}_{dq} - R_{\text{ph}}\boldsymbol{i}_{dq} - \dfrac{\mathrm{d}\boldsymbol{\psi}_{dq}}{\mathrm{d}t}}{\omega_{\text{el}}} \tag{9}$$

by utilizing the voltage, current, and rotor position measurements and/or estimates. Neglecting the rotor angular dependency of the flux linkage by averaging the measurements over several complete rotor rotations [26, p. 25] and by assuming steady-state operation,[3] $\frac{\mathrm{d}\boldsymbol{\psi}_{dq}}{\mathrm{d}t} \approx \boldsymbol{0}$ results. On this basis, (9) can be simplified to

$$\boldsymbol{\psi}_{dq} = \boldsymbol{Q}^{-1}\frac{\boldsymbol{v}_{dq} - R_{\text{ph}}\boldsymbol{i}_{dq}}{\omega_{\text{el}}}. \tag{10}$$

Using (10), the flux linkage combinations can be calculated and are subsequently stored in the RAM (see Section V-A) together with the actual current $\boldsymbol{i}_{dq}$, and the actual winding temperature ϑ. The actual winding temperature is calculated based on the online identified R_{ph}, a reference value R_{ref}—which is measured at reference temperature ϑ_{ref}—and an offline identified relative temperature-dependence coefficient α_{R},[4] by using

$$\vartheta = \frac{1}{\alpha_{\text{R}}}\frac{R_{\text{ph}} - R_{\text{ref}}}{R_{\text{ref}}} + \vartheta_{\text{ref}}. \tag{11}$$

If the offline identified temperature-dependence coefficient of the permanent flux linkage α_ψ is obtained at the same temperature at which α_{R} is determined, it can be assumed that $\vartheta_{\text{m}} \approx \vartheta$ holds in thermal steady state.[5] This assumption allows to use the online tracked winding temperature for the permanent magnets. Therefore, during operation, an offset $\Delta\psi_{\text{PM}}$—caused by a temperature drift $\Delta\vartheta$ of ψ_{PM}—is calculated based on the actual winding temperature. As with the resistance, the calculation of $\Delta\psi_{\text{PM}}$ uses an offline-identified relative gradient of the regression line, i.e., α_ψ, and a reference flux linkage $\psi_{\text{PM,ref}}$ which leads to

$$\Delta\psi_{\text{PM}} = \alpha_\psi\psi_{\text{PM,ref}}\Delta\vartheta. \tag{12}$$

Since ψ_d depends on ψ_{PM}, the flux linkage map on the d-axis is adapted for temperature drifts. Therefore, the flux linkage map, stored in the RAM, is adjusted according to the offset $\Delta\psi_{\text{PM}}$, i.e., whenever the temperature is updated, the ψ_d map is shifted along the ψ_d-axis. Finally, it should be mentioned that the offset is independent of the current combinations. This ensures that the flux linkage map is always up-to-date with regard to the actual temperature.

[3]Detection of steady-state operation in real time is performed by specifying an acceptable degree of deviation (e.g., $\pm 1\%$) of the variables of concern from their nominal value.

[4]Either the temperature-dependence coefficient of the winding material, e.g., copper ($\alpha_{\text{R}} = 0.00393\,1/K$) can be used, or, as it is done in this work, α_{R} is determined offline by measuring the resistance at two defined temperatures.

[5]The assumption applies to almost all small drives due to their low thermal resistance. If this is not valid, an estimation of the rotor temperature is necessary; see, e.g., [32]–[34].

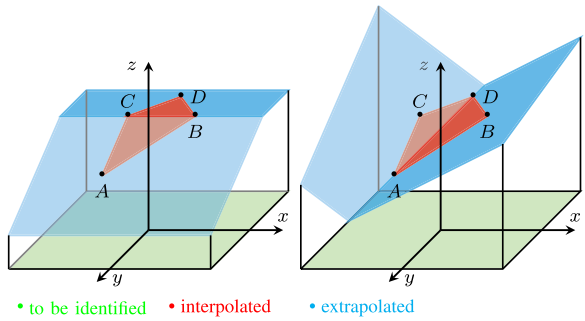

Fig. 2. Schematic interpolation and extrapolation ranges for identification of arbitrary maps based on scattered data sets, including the triangle mesh (shown as red area) on which the gradient calculation is based. Points A, B, C, and D are considered known.

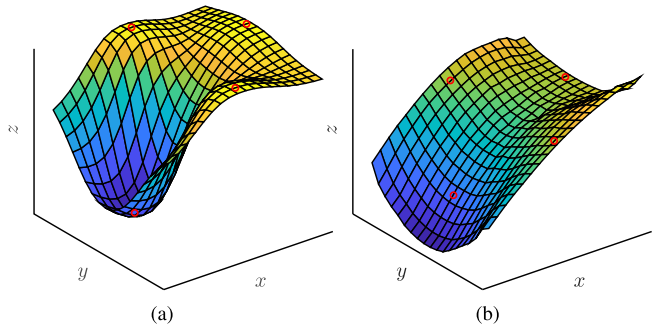

Fig. 3. Schematic solution of the map identification problem using an IDW approach. The red circles are sampled points on which the IDW is based. (a) Conventional IDW approach. (b) Adapted IDW approach.

B. Interpolation and Extrapolation

For the generation of the flux linkage maps, data points are required that describe the (nonlinear) relationship between the stator current and flux linkage. The number of these points should be big enough to sufficiently describe the aforementioned relationship, but also relatively small to avoid increased memory requirements. Hence, due to RAM limitations, the identification algorithm must avoid storing congruent or similar measurements. Therefore, data pairs whose projected distance ε does not exceed a minimum distance threshold $\varepsilon_{\min}$ are merged. The projected distance ε between two arbitrary points in an arbitrary three-dimensional system, with the arbitrary axes x, y, and z, can be described by

$$\varepsilon_i = \sqrt{(x_{i+1} - x_i)^2 + (y_{i+1} - y_i)^2} \tag{13}$$

where x and y can represent i_d and i_q, respectively, while the z-axis can represent any of the flux linkage components (ψ_d or ψ_q).

Following, based on the initial flux linkage calculated with (8), the flux linkage maps are adapted iteratively using the stored data sets. If a minimum number of measured values is stored in the RAM, the identification algorithm starts interpolating between the individual measurements and extrapolating in the outer area toward the map border; see Fig. 2. In doing so, the flux linkage maps cover a wide range of current values, rendering the method useful over a broad span of operating points.

There is a variety of interpolation and extrapolation methods, e.g., spline [31], bicubic spline [35], Kriging [36], [37], radial basis function [27], and several triangle-based methods [38]. However, most of them are quite complex and resource-intensive for real-time implementations. For this purpose, the proposed identification approach uses an inverse distance weighting (IDW) algorithm suitable for interpolation and extrapolation. A detailed description can be found, e.g., in [39]. Using the conventional IDW, the to-be-found z-values are calculated at the pairs of the searched (x, y)-positions using

$$z(x,y) = \frac{\sum \left(\frac{1}{\varepsilon_i}\right)^r z(x_i, y_i)}{\sum \left(\frac{1}{\varepsilon_i}\right)^r}. \tag{14}$$

According to (14), the influence of the measured values in the vicinity of the to-be-found points is inversely proportional to their distance, which is weighted by the factor r.[6] By applying conventional IDW, the solution to the described problem of an unknown surface with four initial scattered values results in a map shown in Fig. 3(a). As can be seen, the calculated surface exhibits strong curvatures and is not monotonically nondecreasing. This behavior is implausible within the scope of flux linkage maps. For this reason, the IDW method is adapted by exploiting the knowledge of the flux linkage behavior. This is done by weighting and averaging the gradient of the surface instead of the z-values themselves. This is reasonable from a physical point of view, since the gradient of the flux linkage maps corresponds to the partial inductances. The latter change only in a monotonic manner, even if the electrical machine is characterized by strong saturation and cross-coupling effects.

Given the above, two steps are required to determine the local surface equations between the scattered measurements. First, a local gradient is calculated at the position of each sample. This procedure corresponds to the formation of a triangular plane defined by a sample and its neighboring points. Considering the possibility of triangular meshing several triangular points may result for a given number of samples. For example, as shown with the red area in Fig. 2, for four sampled points, i.e., A, B, C, and D, four triangles (see $\overset{\triangle}{ABC}$ and $\overset{\triangle}{BCD}$ on the left-hand side as well as $\overset{\triangle}{ACD}$ and $\overset{\triangle}{ABD}$ on the right-hand side of Fig. 2) and thus four local normal vectors result. Note that the latter indicate the surface gradient. As a result, a normal vector $\boldsymbol{n}$ and a known supporting point suffice to establish a plane equation. To this aim, the normal vectors are determined based on the known points of each triangle. For example, the normal vector of the triangle $\overset{\triangle}{ABC}$ at point A is given by

$$\boldsymbol{n} = \boldsymbol{b} \times \boldsymbol{c} \tag{15}$$

where $\boldsymbol{b} = \vec{AB}$ and $\boldsymbol{c} = \vec{AC}$.

[6]Commonly, the distance between the known and to-be-found points is quadratically penalized (i.e., $r = 2$) to reduce the influence of points located further away.

Second, a plausibility check is performed. Due to the fact that the differential inductance cannot be negative, negative components of the gradient are prevented along the main axis (i_d-axis for ψ_d-map, and i_q-axis for ψ_q-map). In doing so, map errors resulting from corrupted measurements are avoided. Finally, after determining the normal vectors for each grid point, the z values are calculated for all grid coordinates with

$$\boldsymbol{n}(x,y) = \frac{\sum \left(\frac{1}{\varepsilon_i}\right)^r \boldsymbol{n}(x_i, y_i)}{\sum \left(\frac{1}{\varepsilon_i}\right)^r}. \tag{16}$$

As can be seen in the above expression, all normal vectors are taken into account according to their distance, i.e., inversely proportional to the distance from the searched grid point. Hence, thanks to the proposed modifications, the adapted IDW approach results in a monotonic flux linkage map, as depicted in Fig. 3(b).

C. Impact of Parameter Uncertainties

To determine the influence of the individual parameters on the identification of ψ_d and ψ_q, the tolerance of the results is determined by estimating the error propagation. For this purpose, the maximum possible error $\Delta\zeta$ given by

$$\Delta\zeta = \sum_{l=1}^{\kappa} \left| \frac{\partial \zeta}{\partial w_l} \Delta w_l \right| \tag{17}$$

can be calculated based on the partial derivatives of the variable of concern, i.e., ζ, after w with respect to the number of parameters κ in the system.[7] More concretely, for calculating the maximum measurement error, i.e., $\Delta\psi_{d,\zeta}$ and $\Delta\psi_{q,\zeta}$, (10) is partially differentiated with respect to each of the varying parameters, i.e., R_{ph}, $\boldsymbol{i}_{dq}$, $\boldsymbol{v}_{dq}$, and ω_{el}, which leads to

$$\frac{\partial \psi_d}{\partial R_{\mathrm{ph}}} = -\frac{i_q}{\omega_{\mathrm{el}}}, \quad \frac{\partial \psi_q}{\partial R_{\mathrm{ph}}} = \frac{i_d}{\omega_{\mathrm{el}}} \tag{18a}$$

$$\frac{\partial \psi_d}{\partial i_q} = -\frac{R_{\mathrm{ph}}}{\omega_{\mathrm{el}}}, \quad \frac{\partial \psi_q}{\partial i_d} = \frac{R_{\mathrm{ph}}}{\omega_{\mathrm{el}}} \tag{18b}$$

$$\frac{\partial \psi_d}{\partial v_q} = \frac{1}{\omega_{\mathrm{el}}}, \quad \frac{\partial \psi_q}{\partial v_d} = -\frac{1}{\omega_{\mathrm{el}}} \tag{18c}$$

$$\frac{\partial \psi_d}{\partial \omega_{\mathrm{el}}} = -\frac{v_q - R_{\mathrm{ph}} i_q}{\omega_{\mathrm{el}}^2}, \quad \frac{\partial \psi_q}{\partial \omega_{\mathrm{el}}} = \frac{v_d - R_{\mathrm{ph}} i_d}{\omega_{\mathrm{el}}^2}. \tag{18d}$$

Hence, with (18), the maximum possible error for each flux linkage component is calculated with

$$\begin{aligned}\Delta\boldsymbol{\psi}_{dq,\zeta} = &\left| \boldsymbol{Q} \frac{\boldsymbol{i}_{dq}}{\omega_{\mathrm{el}}} \Delta R_{\mathrm{ph}} \right| + \left| \frac{R_{\mathrm{ph}}}{\omega_{\mathrm{el}}} \boldsymbol{Q} \Delta \boldsymbol{i}_{dq} \right| \\ &+ \left| -\frac{1}{\omega_{\mathrm{el}}} \boldsymbol{Q} \Delta \boldsymbol{v}_{dq} \right| + \left| -\frac{\boldsymbol{\psi}_{dq}}{\omega_{\mathrm{el}}} \Delta\omega_{\mathrm{el}} \right|. \end{aligned} \tag{19}$$

The course of the maximum measurement error determined from error propagation is shown in Fig. 4 for motor M4, the parameters of which are provided in Table III. Analyzing (19) and by visual inspection of Fig. 4, the following assessment can be made for the measurement uncertainty of the flux linkage identification.

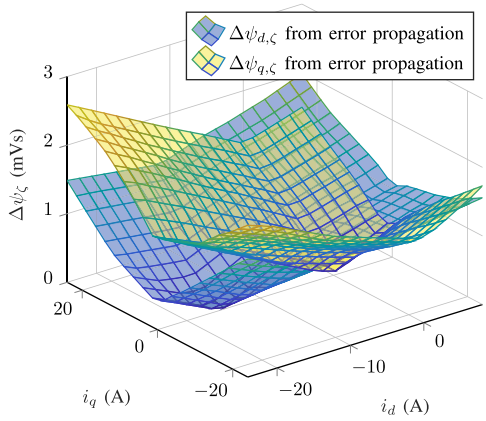

Fig. 4. Typical course of the maximum measurement error determined from error propagation on the example of motor M4. For a better understanding of the possible error, Fig. 5 shows the identified flux linkage.

1) It gets bigger with increasing current due to the uncertainty in the estimated resistance.
2) It increases with decreasing speed due to the decreasing induced voltage, which in turn is measured in a very poor measuring range.
3) It is adversely affected by unmodeled effects, i.e., higher order harmonics and iron losses. Specifically, it increases at higher speeds due to the increasing influence of iron losses. For this reason, a speed range of $\omega_{\mathrm{m}} \in [5, 20]\,\%$ of the nominal speed is recommended for the test machines under consideration. Note that in order to be able to use the proposed online identification method also at higher speeds, an additional term must be included in (10) to account for the iron losses—if pronounced—during steady state, e.g., by using a voltage error term [26, p. 25], or a parallel resistance [40]–[42].
4) It increases as the measurement/estimate of the rotor angle becomes less accurate. An insufficient phase shift correction—which is necessary for the compensation of the voltage-measurement filter—as well as an increasing misalignment of the rotor position due to frictional effects, introduces inaccuracies in the transformation from the three-phase to the dq-plane; see (1).

Notwithstanding the above, when considering the aforediscussed influencing factors, any nonlinearities in the flux linkage can be relatively easily identified online and used to optimize the prediction accuracy. Fig. 5 shows the identified flux linkage maps for test motors M3 and M4 (see Table III). As can be seen, the initially assumed linear machine model can be optimized in real time during operation. Finally, implementation details and further relevant information are provided in Section V.

IV. Flux Linkage-Based Direct Model Predictive Current Control With Variable Switching Point

The main control objective of the presented VSP^{2}CC method is to reduce the current ripple during steady-state operation.

[7] Note that (17) represents the worst-case scenario in which the individual measurement deviations Δw do not compensate for each other.

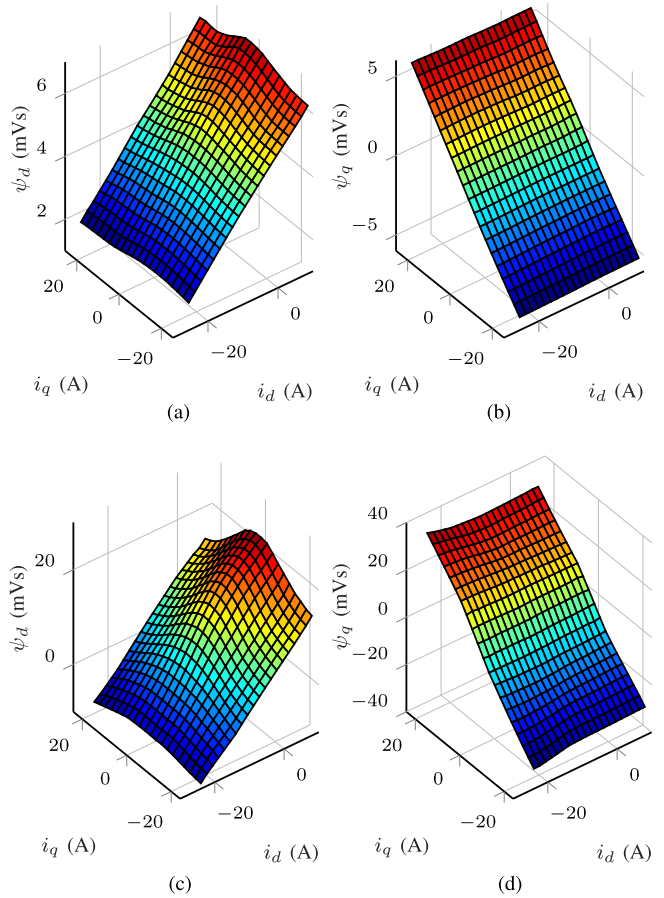

Fig. 5. Identified flux linkage maps with 20×20 grid points. (a) $\psi_d(i_d, i_q)$ for motor M3. (b) $\psi_q(i_d, i_q)$ for motor M3. (c) $\psi_d(i_d, i_q)$ for motor M4. (d) $\psi_q(i_d, i_q)$ for motor M4.

Moreover, the controller has to exhibit very fast dynamic behavior to quickly tackle changes in the current references [15]. To this end, the optimization problem decides in real time whether one switch position is applied for the whole control interval (similar to the conventional FCS-MPC), or a VSP with a combination of two switch positions is implemented instead. Furthermore, as shown in the sequel, by utilizing the proposed flux linkage maps in the prediction process, the proposed controller is suitable for nonlinear machines and significantly improves their overall performance. Algorithm 1 shows the pseudocode of the discussed MPC method.

A. Preselection Based on the Deadbeat Control Action

To keep the computational complexity of the proposed direct MPC method modest [4] so as to render its real-time implementation with the desired (high) control frequencies possible, a preselection method—introduced as "heuristic preselection" in [7]—is employed.[8] This method utilizes the deadbeat control action so as to reduce the search space. As a result, instead of evaluating eight candidate switch positions (i.e., seven SVs) at each prediction step, only four candidate switch positions (i.e., three unique SVs) are taken into consideration. The deadbeat solution is given by

$$\boldsymbol{v}_{dq,\mathrm{db}}(k) = \boldsymbol{L}\frac{\boldsymbol{i}^*_{dq}(k) - \boldsymbol{i}_{dq}(k)}{T_{\mathrm{cf}}} + R_{\mathrm{ph}}\boldsymbol{i}_{dq}(k) + \omega_{\mathrm{el}}(k)\left(\boldsymbol{Q}\boldsymbol{L}\boldsymbol{i}_{dq}(k) + \begin{bmatrix} 0 \\ \psi_{\mathrm{PM}} \end{bmatrix}\right). \tag{20}$$

With (20), the angle of the desired voltage vector $\boldsymbol{v}_{dq,\mathrm{db}}(k)$ that drives the current to its reference within one control interval T_{cf} can be found with

$$\gamma(k) = \arctan2(\boldsymbol{v}_{dq,\mathrm{db}}(k)) + \varphi, \{\gamma \in \mathbb{R} \mid 0 \leq \gamma < 2\pi\}. \tag{21}$$

Depending on the angle γ of the deadbeat solution (20), the triangular sector (one out of the six) wherein $\boldsymbol{v}_{dq,\mathrm{db}}(k)$ lies is found. Thus, only two active and two zero SVs that form the sector are candidate solutions, as presented in Table I.

TABLE I
CANDIDATE VOLTAGE SVS DEPENDING ON $\gamma(k) = \angle\boldsymbol{v}_{dq,\mathrm{db}}(k)$

γ	Sector	SVs
$[0, \frac{\pi}{3}]$	I	$\boldsymbol{v}_1, \boldsymbol{v}_2, \boldsymbol{v}_{0/7}$
$[\frac{\pi}{3}, \frac{2\pi}{3}]$	II	$\boldsymbol{v}_2, \boldsymbol{v}_3, \boldsymbol{v}_{0/7}$
$[\frac{2\pi}{3}, \pi]$	III	$\boldsymbol{v}_3, \boldsymbol{v}_4, \boldsymbol{v}_{0/7}$
$[\pi, \frac{4\pi}{3}]$	IV	$\boldsymbol{v}_4, \boldsymbol{v}_5, \boldsymbol{v}_{0/7}$
$[\frac{4\pi}{3}, \frac{5\pi}{3}]$	V	$\boldsymbol{v}_5, \boldsymbol{v}_6, \boldsymbol{v}_{0/7}$
$[\frac{5\pi}{3}, 2\pi]$	VI	$\boldsymbol{v}_6, \boldsymbol{v}_1, \boldsymbol{v}_{0/7}$
Equivalence between voltage SVs and switch positions		
$\boldsymbol{v}_0 \equiv [-1\,-1\,-1]^T$, $\boldsymbol{v}_1 \equiv [1\,-1\,-1]^T$, $\boldsymbol{v}_2 \equiv [1\,1\,-1]^T$, $\boldsymbol{v}_3 \equiv [-1\,1\,-1]^T$ $\boldsymbol{v}_4 \equiv [-1\,1\,1]^T$, $\boldsymbol{v}_5 \equiv [-1\,-1\,1]^T$, $\boldsymbol{v}_6 \equiv [1\,-1\,1]^T$, $\boldsymbol{v}_7 \equiv [1\,1\,1]^T$		

B. VSP²CC With Inductance-Based Prediction Model

The VSP²CC algorithm presented in [15] evaluates the evolution of the stator currents based on (5) for different combinations of the three unique candidate SVs over a horizon of N_{p} steps. For the first prediction step, the three candidate SVs are evaluated by taking into account two possibilities, namely, either one SV is applied to the inverter for the whole T_{cf} (i.e., similar to the conventional FCS-MPC), or two SVs are implemented within one T_{cf} by introducing one VSP t_{z}, with $0 < t_{\mathrm{z}} < T_{\mathrm{cf}}$. For the prediction steps further in the horizon, i.e., $N_{\mathrm{p}} > 1$, however, the concept of standard FCS-MPC is employed, meaning that only three candidate solutions are considered from the second step of the horizon onwards. In doing so, the computational complexity is kept at bay, since the total number of candidate solutions to be enumerated is $3^{N_{\mathrm{p}}+1}$. This number is significantly smaller than $3^{2N_{\mathrm{p}}}$ which is the number of candidate solutions in case one VSP is introduced at each prediction step. Hence, the adopted concept facilitates the real-time implementation of the proposed VSP²CC method, as shown in Section V.

The computation of the VSP t_{z} in the first prediction step is based on the calculation of the current gradients for i_d and i_q. To this aim, the following assumptions are made.

[8]Note that even though such an approach may lead to suboptimal results [4], the results acquired with the proposed method (see Section VI) do not impact optimality.

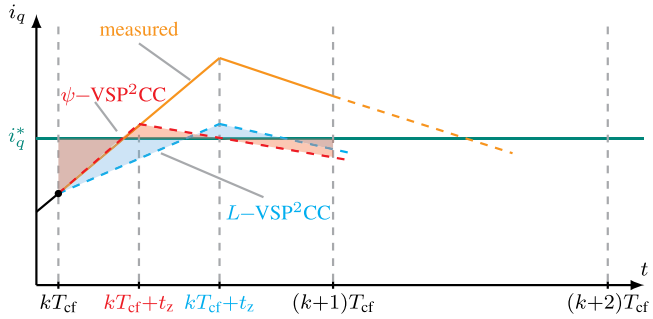

Fig. 6. Flux linkage- and inductance-based VSPs t_z resulting by the intersection of two possible trajectories of the q-component of the stator current $\boldsymbol{i}_{dq}$. The measured current is obtained when L-VSP^{2}CC is used while saturation occurs. For simplicity, only the q-component of the current is shown.

1) Due to the very small T_{cf} (i.e., 10 μs), the saturation does not affect the slopes during one control interval T_{cf}. Therefore, the slopes are assumed to be piecewise linear.
2) The rotor angle φ is kept constant during one interval T_{cf}.[9] Note that the possible values of the stator voltage (2) are updated at each prediction step.
3) Nonlinear time-varying parameters, such as R_{ph}, ψ_{PM}, and ω_{m}, do not affect the current slopes due to the significantly larger associated time constants as compared with T_{cf}.

Taking into account the above assumptions, the piecewise constant current slopes over one T_{cf} are given by [6], [43], [44]

$$\boldsymbol{m}_{dq}(k) = \frac{\boldsymbol{i}_{dq}(k+1) - \boldsymbol{i}_{dq}(k)}{T_{\text{cf}}} = \frac{\Delta \boldsymbol{i}_{dq}(k)}{T_{\text{cf}}}. \tag{22}$$

Moreover, the aforementioned assumptions imply that the current slopes at time steps k and $k+1$ are the same. By denoting these slopes with the subscripts n_1 and n_2, respectively, the rms current error on the d- and q-axis over one control interval T_{cf} is [7]

$$e_{\text{rms}^2,n_1,n_2(t_z)} = \frac{1}{T_{\text{cf}}}\left(\int_0^{t_{z,n_1,n_2}} \|\boldsymbol{i}_{dq,0} + \boldsymbol{m}_{dq,n_1} t - \boldsymbol{i}_{dq}^*\|_2^2 \,\mathrm{d}t + \int_{t_{z,n_1,n_2}}^{T_{\text{cf}}} \|\boldsymbol{i}_{dq,t_z} + \boldsymbol{m}_{dq,n_2} t - \boldsymbol{i}_{dq}^*\|_2^2 \,\mathrm{d}t \right) \tag{23}$$

where $\boldsymbol{i}_{dq}^*$ is the reference value of the stator current. An illustrative example of the resulting error area is shown in Fig. 6. Expression (23) is calculated for each voltage SV combination for the first step of the prediction horizon, i.e., nine combinations in total. The variable switching point t_{z,n_1,n_2}, which minimizes the current ripple for each SV combination, can be obtained by setting the derivative of (23) equal to zero, i.e., $\mathrm{d}e_{\text{rms}^2}/\mathrm{d}t_z = 0$. This yields

$$t_{z,n_1,n_2} = T_{\text{cf}} \frac{a_{n_1,n_2} + b_{n_1,n_2}}{c_{n_1,n_2} + d_{n_1,n_2}} \tag{24}$$

[9]For machines with many pole pairs, the variation of the rotor position within one T_{cf} may affect the VSP calculation at high speeds. For example, when $n_{\text{m}} = 4000$ rpm, $p = 4$, and $T_{\text{cf}} = 10\,\mu$s, the rotor position change is $\varphi \approx 0.017$ rad in one T_{cf}, leading to a possible voltage variation up to 1.8 %.

where

$$\begin{aligned} a_{n_1,n_2} &= (\Delta i_{d,n_2} - \Delta i_{d,n_1})(2i_d - 2i_d^* + \Delta i_{d,n_2}) \\ b_{n_1,n_2} &= (\Delta i_{q,n_2} - \Delta i_{q,n_1})(2i_q - 2i_q^* + \Delta i_{q,n_2}) \\ c_{n_1,n_2} &= (\Delta i_{d,n_1} - \Delta i_{d,n_2})(2\Delta i_{d,n_1} - \Delta i_{d,n_2}) \\ d_{n_1,n_2} &= (\Delta i_{q,n_1} - \Delta i_{q,n_2})(2\Delta i_{q,n_1} - \Delta i_{q,n_2}). \end{aligned}$$

Observing (24), it is evident that when the same voltage SV is evaluated for both time steps k and $k+1$, the current slope remains constant over the whole T_{cf}. This implies that the associated switching time is $t_{z,n_1,n_2} = 0$, i.e., only one switch position $\boldsymbol{u}_{abc}$ is applied within one T_{cf}. As a result, either one switch transition occurs within T_{cf}, or switching is avoided altogether in case the previously applied switch position is the same. Furthermore, it should be mentioned that voltage SV combinations that lead to current trajectories that do not intersect at all within T_{cf}, or lead to $t_{z,n_1,n_2} > T_{\text{cf}}$, are excluded as infeasible.

C. VSP^{2}CC With Flux Linkage Map-Based Prediction Model

In contrast to [15], the flux linkage is used for the current prediction in this work. To this end, the following expressions are utilized:

$$f_\psi : \mathbb{R}^2 \to \mathbb{R}^2, (i_d, i_q) \to (\psi_d, \psi_q) \tag{25a}$$

$$f_\psi^{-1} : \mathbb{R}^2 \to \mathbb{R}^2, (\psi_d, \psi_q) \to (i_d, i_q). \tag{25b}$$

First, (25a) is used to map the current $\boldsymbol{i}_{dq}(k+\ell-1)$, with $\ell = 1, \ldots, N_p$, into the corresponding flux linkage. This procedure is done only once after the current measurement. Second, the predicted flux linkage is computed with (7). Subsequently, (25b) is used to get $\boldsymbol{i}_{dq}(k+\ell)$. The procedure of the reverse mapping is performed after each individual prediction step, since the optimization problem underlying VSP^{2}CC (see Section IV-D) optimizes the current behavior. Thanks to the utilization of the flux linkage maps and the decoupling of the prediction process from the system inductances, an optimized gradient calculation can be acknowledged, especially when considering nonlinear PMSMs. This is exemplified in Fig. 6, where the current trajectory computed with the inductance-based prediction model (5) results in a suboptimal t_z, causing an unnecessary high current ripple, as compared with that computed with the proposed method.

As explained in Section III, the nonlinear functions f_ψ and f_ψ^{-1} are stored in flux linkage maps and identified online during operation. At this point, an important distinction must be made when using the online parameter identification method, as each map exists in two copies, i.e., in the RAM of the processor and the FPGA. Regarding the former, the flux linkage maps in the RAM are accessed by the processor and are modified in a time-uncritical task with the identification procedure described in Section III. However, since the prediction procedure and the subsequent optimization process are fully implemented on the FPGA, the maps are also stored there so that can be directly used without introducing any communication delays. This, however, may tax the computational and memory resources required for the proposed algorithm. To address this, methods that alleviate

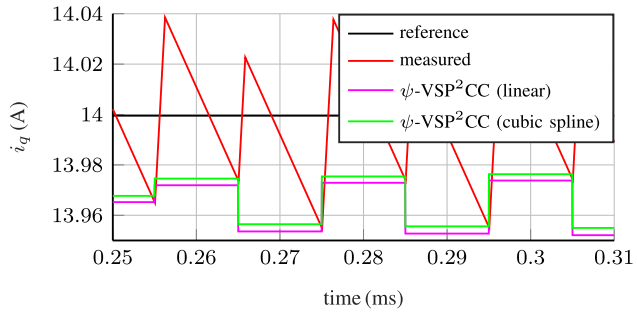

Fig. 7. Motor M3: Comparison of interpolation methods for prediction using $i_d^* = -1\,\text{A}$, $i_q^* = 14\,\text{A}$ at steady state with a speed of $n_\text{m} = 100$ rpm.

the computational load are implemented, as explained in the sequel.

1) Interpolation: The online identification of the flux linkage maps is performed on a processor in a time-uncritical manner by—theoretically—using any kind of interpolation and extrapolation methods, e.g., IDW or cubic spline. For the FPGA implementation, however, interpolation and extrapolation are relatively complex.[10] For this reason, the use of linear interpolation is recommended due to its resource efficiency and dramatically reduced calculation time inside the FPGA, as shown in Section V-B. Moreover, as can be seen in Fig. 7, such an interpolation method is accurate enough despite its simplicity. When considering the test motor M3 (see Table III), a 16×16 map and a current range of $[-20, 20]$ A, the maximum deviation is 3 mA, which is negligible for the considered measurement range. Hence, no performance deterioration is observed comparing with the cubic spline method.

2) Extrapolation: Considering resource efficiency and control frequencies of $f_\text{cf} = 100\,\text{kHz}$ (with $f_\text{cf} = 1/T_\text{cf}$), extrapolation on the FPGA is complex and thus it is better to be avoided. Since, for reasons explained above, only interpolation is performed on the FPGA, the resulting flux linkage maps must cover the entire measurement range to allow for prediction of the current trajectories over the whole operating current range. For this reason, the maps are generated in the processor using both interpolation and extrapolation so as to cover the whole measurement range of the current sensors as described in Section III. Following, these maps are transferred from the processor to the FPGA during operation so that they will be available for all the steps of the prediction process. Hence, not performing extrapolation on the FPGA during the prediction has no adverse effects since the required information is readily available.

[10]Note that an option to avoid interpolation altogether is to use flux linkage maps with a very big number of sampling points. In this way, (valuable) digital signal processing (DSP) slices needed for interpolation on the FPGA remain available for other functionalities; see Section V-B. However, as mentioned before, storing these points in the RAM is not practical due to the very long latency associated with the memory access. Storing them in the FPGA registers is also a poor choice from an implementation point of view since a significant amount of resources would be required for an acceptable degree of granularity. For example, considering the chip in Section V, all available look-up tables (LUTs) of the FPGA would be used for one 256×256 map. Maps with lower granularity, e.g., a 100×100 map, would result in a granularity of 400 mA for a current range of $[-20, 20]$ A, which is not accurate enough. It is therefore preferred to use linear interpolation instead.

D. Optimization Problem

The cost function is designed such that to minimize the current ripple while controlling the switching frequency. Moreover, it should take into account the possibility of applying one or two voltage SVs (i.e., switch positions) in the first prediction horizon step. On this basis, the formulated cost function to be minimized in real time is[11]

$$J(k) = \sum_{\ell=k}^{k+N_\text{p}-1} \Big(\|\mathbf{y}^*(\ell+1) - \mathbf{y}(\ell+1)\|_2^2 + \hat{f}(\boldsymbol{i}_{dq}(\ell+1)) + \lambda_\text{u} \|\boldsymbol{\Delta}[\bar{\boldsymbol{u}}_{abc}^T(\ell-1)\bar{\boldsymbol{u}}_{abc}^T(\ell)]^T\|_1 \Big) \tag{26}$$

where

$$\hat{f}(\boldsymbol{i}_{dq}(\ell+1)) = \begin{cases} 4 & \text{if } \|\boldsymbol{i}_{dq}(\ell+1)\|_2 > i_\text{max} \\ 0 & \text{if } \|\boldsymbol{i}_{dq}(\ell+1)\|_2 \leq i_\text{max} \end{cases} \tag{27}$$

with $\mathbf{y}^* = [\boldsymbol{i}_{dq}^{*T} \boldsymbol{i}_{dq}^{*T}]^T \in \mathbb{R}^4$ being the reference vector and $\mathbf{y} = [\boldsymbol{i}_{dq,\text{t}_\text{z}}^T \boldsymbol{i}_{dq,\text{T}_\text{cf}}^T]^T \in \mathbb{R}^4$ the output vector. The sequence of manipulated switch positions over a finite horizon of $N_\text{p} \in \mathbb{N}^+$ time steps is defined as

$$\boldsymbol{U}(k) = [\bar{\boldsymbol{u}}_{abc}^T(k)\bar{\boldsymbol{u}}_{abc}^T(k+1)\ldots\bar{\boldsymbol{u}}_{abc}^T(k+N_\text{p}-1)]^T \in \mathbb{U} \tag{28}$$

where $\bar{\boldsymbol{u}}_{abc} = [\boldsymbol{u}_{abc,0}^T \boldsymbol{u}_{abc,\text{t}_\text{z}}^T]^T$ and $\mathbb{U} = \{-1, 1\}^{6N_\text{p}}$. Moreover, $\boldsymbol{\Delta}[\bar{\boldsymbol{u}}_{abc}^T(\ell-1)\bar{\boldsymbol{u}}_{abc}^T(\ell)]^T$ with $\boldsymbol{\Delta} = \begin{bmatrix} \mathbf{0} & -\boldsymbol{I} & \boldsymbol{I} & \mathbf{0} \\ \mathbf{0} & \mathbf{0} & -\boldsymbol{I} & \boldsymbol{I} \end{bmatrix}$, where $\mathbf{0}$ and $\boldsymbol{I}$ are, respectively, the zero and identity matrices of appropriate dimensions (here 3×3), denotes the penalization of the control action, and consequently, of the switching frequency, which is weighted by $\lambda_\text{u} > 0$. Finally, (27) represents a hard constraint on the stator current, implemented as a protection mechanism, with "4" being the maximum current in per unit (p.u.).[12]

Inspecting (26), it can be seen that the cost function is designed to account for both possibilities when solving the VSP^{2}CC problem, namely that either two or one switch positions can be implemented within one control interval T_cf. In the former case, the algorithm uses the pair of switch positions (i.e., voltage SVs) and the corresponding current errors of i_q and i_d which are calculated at the time instants t_z and T_cf, respectively. In the latter case, due to $t_\text{z} = 0$, the first current term of (26) for $\boldsymbol{i}_{dq}$ uses the same current error as the second term at T_cf in order to enable a comparable cost, i.e., $\boldsymbol{i}_{dq,\text{t}_\text{z}} = \boldsymbol{i}_{dq,\text{T}_\text{cf}}$. Furthermore, in contrast to the cost function in [15], (26) uses the squared ℓ_2-norm for the tracking errors to avoid any closed-loop stability issues as well as for performance improvement [45]. Finally, since the d-axis current is not controlled to zero when IPMSMs are of

[11]Note that, in order to reduce the switching frequency (and thus the switching losses), while keeping the computational load modest, the reference tracking error term is calculated only for one zero voltage SV (i.e., $\boldsymbol{v}_0$), whereas the switching error term considers both $\boldsymbol{v}_0$ and $\boldsymbol{v}_7$. Following, the zero voltage SV that results in less switching effort—with respect to the previously applied voltage SV—is chosen.

[12]Theoretically, a soft constraint is to be preferred since it can avoid feasibility problems when solving (26).

concern, the current limit (27) is based on the amplitude of the stator current.

With cost function (26) and the mapping functions (25a) and (25b), the VSP^{2}CC problem is stated as

$$\begin{aligned} &\underset{\bar{\boldsymbol{u}}_{abc} \in \mathbb{U}}{\text{minimize}} \quad J \text{ (see (26))} \\ &\text{subject to} \quad \text{(25a), (25b), (27).} \end{aligned} \tag{29}$$

Solving (29) yields the optimal switch position(s) $\bar{\boldsymbol{u}}_{abc,\text{opt}}$ which is (are) to be applied at the corresponding optimal switching time instant(s), i.e., $t = 0$ and/or $t_{\text{z,opt}}$. Note that according to the receding horizon policy, the elements of the switching sequence $\boldsymbol{U}$ that correspond to the predictions steps $N_\text{p} \geq 2$ are discarded. In doing so, feedback is provided and a degree of robustness to system uncertainties is achieved [46].

E. Assessment of Influencing Factors

The utilization of the flux linkage maps in the prediction process, i.e., the ψ-based—in comparison to the L-based [15]—prediction, is particularly advantageous for (small) drives with saturation and cross-coupling effects for several reasons. More specifically, MPC with an L-based prediction model suffers from the following pitfalls.

1) The bigger the phase resistance R_ph, as is the case, e.g., with small motors (ironless winding), the bigger the voltage drop across it. This, in turn, can lead to a significant prediction error. Since in case of the L-based prediction the inductance appears in the denominator of (5), a decrease in it results in an underestimated voltage drop across R_ph. A reduced inductance due to saturation, e.g., by half, erroneously leads to a predicted voltage drop across R_ph, which is half than it actually is.
2) The larger the ratio between L_d and L_q, the more significant the prediction error when saturation happens. However, if the ratio remains constant over the entire operating range, such effects may cancel each other in the term $\omega_\text{el}\boldsymbol{L}$ of (5).
3) For inductances that are almost equal ($L_d \approx L_q$), the impact of ω_el on the prediction error is nonexistent on the d-axis and relatively small on the q-axis.
4) Assuming a constant ϑ_m, the lower the ω_el is, the bigger the prediction error. This is due to a lower back-emf voltage at low speed which leads to a more significant voltage drop across the resistance and inductances. In other words, the increased current change causes an increase in the prediction error within one T_cf. This, however, as mentioned above, affects only the q-axis.
5) The less ψ_d is affected by ψ_PM, i.e., more reluctance difference, the bigger the prediction error on the q-axis.
6) For a given IPMSM and saturation effect, the prediction error increases with a longer control interval T_cf or higher dc-link voltage V_dc.

The impact of several parameter mismatches on L-VSP^{2}CC is experimentally evaluated in Fig. 8 for motor M1; see Table III. As can be seen, the current THD I_THD of DMPC is mostly adversely affected by an inductance inaccuracy, with saturation (i.e., $0.5L$) indicating the worst-case scenario. More precisely, if the inductance is used in the prediction model and it is halved due to saturation in the real-world system (i.e., the machine), the electrical time constant τ_el is also halved resulting in an actual current which is double than its predicted value. Similar results have been reported in, e.g., [47], for conventional DMPC. The proposed ψ-VSP^{2}CC, however, avoids such pitfalls, enabling a more accurate calculation of the current trajectories, and, consequently, of VSPs, thanks to which the current ripple can be significantly decreased (see Section VI). The main benefit of ψ-VSP^{2}CC is also visualized in Fig. 6, where the positive effect of an improved current prediction accuracy is exemplified.

Algorithm 1: Flux Linkage-Based VSP^{2}CC.

function $\bar{\boldsymbol{u}}_{\text{abc,opt}}, t_{\text{z,opt}} = \psi$-VSP^{2}CC($\boldsymbol{i}_{dq}$, φ, N_p, ω_el, V_dc)
  $\boldsymbol{\psi}_{dq}(k-1) \leftarrow \boldsymbol{i}_{dq}(k-1)$ using (25a)
  $\boldsymbol{\psi}_{dq}(k) \leftarrow$ predict using (7) ▷delay time comp.
  $\boldsymbol{i}_{dq}(k) \leftarrow \boldsymbol{\psi}_{dq}(k)$ using (25b)
  $\boldsymbol{v}_{dq,\text{db}}(k) \leftarrow$ deadbeat solution using (20) ▷search space reduction
  $\gamma(k) \leftarrow \angle \boldsymbol{v}_{dq,\text{db}}(k)$ using (21) ▷sector of candidate $\boldsymbol{v}_{dq}(k)$
  for $\ell = 1, \ldots, N_\text{p}$ **do**
    $\boldsymbol{v}_{dq}(k+\ell-1) \leftarrow$ based on $\varphi(k+\ell-1)$ and $V_\text{dc}(k)$ ▷three candidate SVs based on $\gamma(k)$
    for $j = 1, \ldots, 3$ **do** ▷one SV within T_cf
      $\boldsymbol{\psi}_{dq,j}(k+\ell) \leftarrow$ predict using (7)
      $\boldsymbol{i}_{dq,j}(k+\ell) \leftarrow \boldsymbol{\psi}_{dq,j}(k+\ell)$ using (25b)
      $\|\boldsymbol{i}_{dq,j}(k+\ell)\| \leftarrow \boldsymbol{i}_{dq,j}(k+\ell)$ using (27) ▷current constraint
      if $\ell = 1$ **then**
        $\boldsymbol{m}_j(k+\ell) \leftarrow$ using (22) ▷$\boldsymbol{i}_{dq}$ gradients
      end if
    end for
    if $\ell = 1$ **then** ▷VSP for $N_\text{p} = 1$
      for $n_1 = 1, \ldots, 3$ **do**
        for $n_2 = 1, \ldots, 3$ **do**
          if $n_1 = n_2$ **then** ▷one SV within T_cf
            $\boldsymbol{i}_{dq,n_1,n_2}(k+\ell) \leftarrow \boldsymbol{i}_{dq,j}(k+\ell)$
          else ▷VSP for two SVs
            $t_{\text{z},n_1,n_2}(k+\ell) \leftarrow$ (24) ▷VSP
            $\boldsymbol{\psi}_{dq,n_1,n_2}(k+\ell) \leftarrow$ predict with (7)[13]
            $\boldsymbol{i}_{dq,n_1,n_2}(k+\ell) \leftarrow \boldsymbol{\psi}_{dq,n_1,n_2}(k+\ell)$
            $\|\boldsymbol{i}_{dq,n_1,n_2}(k+\ell)\| \leftarrow$ $\boldsymbol{i}_{dq,n_1,n_2}(k+\ell)$ using (27) ▷current constraint
          end if
        end for
      end for
    end if
    $\bar{\boldsymbol{u}}_{abc,\text{opt}}(k), t_{\text{z,opt}}(k) \leftarrow$ solve (29)
  end for
end function

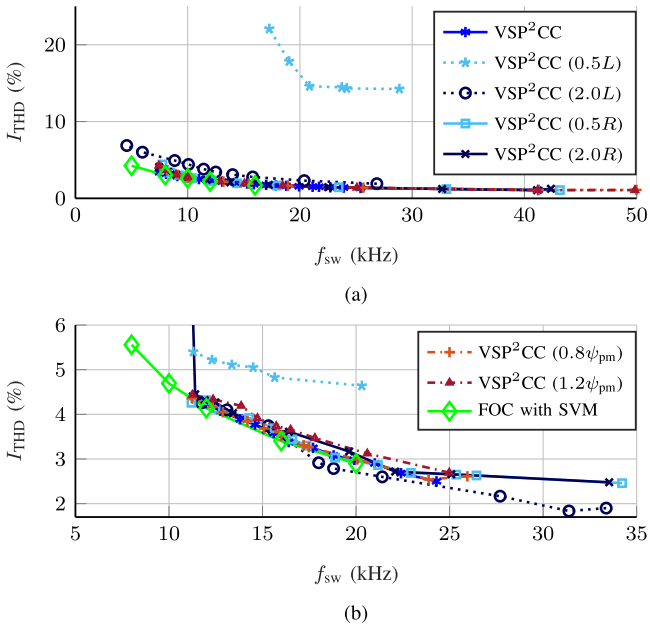

Fig. 8. Motor M1: Trade-off between stator current I_{THD} and f_{sw} with different parameter mismatches for N_{p}=2 with f_{cf}=100 kHz (experimental results). (a) $i_d^* = 0\,\text{A}, i_q^* = 5.0\,\text{A}, n_{\text{m}} = 200\,\text{rpm}$. (b) $i_d^* = 0\,\text{A}, i_q^* = 12.16\,\text{A}, n_{\text{m}} = 3000\,\text{rpm}$.

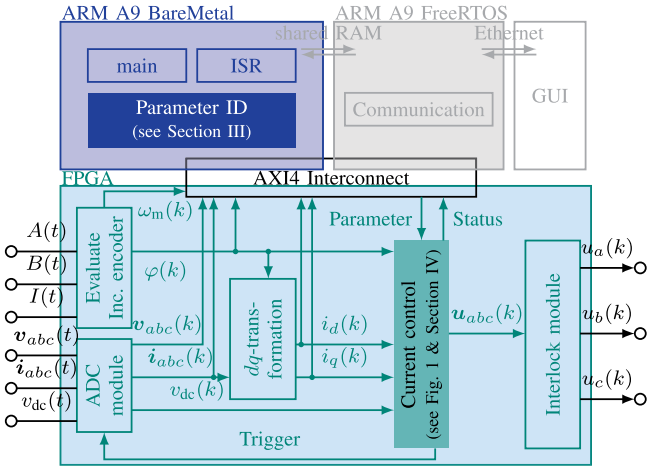

Fig. 9. Schematic representation of the heterogeneous calculation platform with interaction between BareMetal and FPGA.

Finally, it is worth mentioning that a mismatch in R_{ph} and/or ψ_{PM} may negatively affect the reference tracking behavior of all DMPC methods, i.e., an offset occurs, especially at higher speeds. Even though this adverse impact may be small for the investigated machines, it can be addressed by the proposed algorithm since deviations due to temperature changes are tracked and updated online; see Section III-A.

V. Implementation of Heterogeneous Algorithms

New and powerful heterogeneous calculation platforms become more and more popular as well as affordable, as shown, e.g., in [48]. The main advantage of such solutions is the implementation of the time uncritical—but yet complex—parts of an algorithm on a processor, whereas the time critical parts that can be parallelized are implemented on an FPGA by using high clock frequencies with low jitter and low latency [3], [49]; see Fig. 9. Splitting an algorithm into routines and procedures based on their best possible execution is thus recommended. On this basis, such an implementation approach is adopted in this work. Specifically, the parameter identification and flux linkage map adaption, as shown in Section III, are performed on the processor. In contrast, the current control loop (see Section IV) is implemented exclusively on the FPGA along with the analog-to-digital (ADC) oversampling, interlock times, and other smaller tasks, as explained in the following.

A. Platform and Test Bench

The proposed evaluation uses a Zynq-7000 (XC7Z020) SoC FPGA in combination with the HDL-Coder from MathWorks, as described in [3] and [15]. Two ARM A9 processors exist. One of the processors runs a FreeRTOS operating system for communication tasks. The other runs BareMetal, which provides an interrupt service routine (ISR) with $f_{\text{cc}} = 10$ kHz. The BareMetal core reads in the ISR all measurements from the FPGA, detects steady-state operation, and calculates the flux linkage changes, as described in Section III-A. In addition, the flux linkage maps are adapted in the main routine in a time-uncritical manner, whereby the interpolation/extrapolation methods (e.g., IDW) can be used; see Section III-B. The processor parameterizes the MPC algorithm implemented on the FPGA by writing the references and parameters, i.e., R_{ph}, flux linkage maps, λ_{u}.

The MPC algorithm is entirely implemented on the FPGA with a sampling/current control frequency of $f_{\text{cf}} = 100$ kHz. To fully utilize the resources of the control platform as well as to implement the controller in a computationally efficient manner, the following principles are adopted. First, slow time-varying calculations are outsourced to the ISR—which runs in the processor—to save resources. For example, the denominator in (7) indicates the need to perform a division which is a computationally demanding task for the FPGA. However, since the denominator depends on the speed, it can be assumed to be constant within several T_{cf}. Hence, to avoid the division, the reciprocal value of the denominator is calculated on the processor and fed into the FPGA at the beginning of the prediction/optimization procedure.

Second, for divisions that cannot be outsourced to the processor, and thus have to be done on the FPGA, a cautiously chosen bit size is used to keep the required computational resources modest. This applies, e.g., to the division in (24).

Third, efficient resource streaming and sharing is implemented on the FPGA. Therefore, subsequent prediction steps use the resources of the previous steps. Furthermore, as explained in Section IV-C, the flux linkage maps used in the prediction process are fully implemented on the FPGA and are updated by the processor by using the flux linkage maps stored in the RAM. Since the use of such maps is more resource-intensive compared to a simple multiplication that an inductance-based

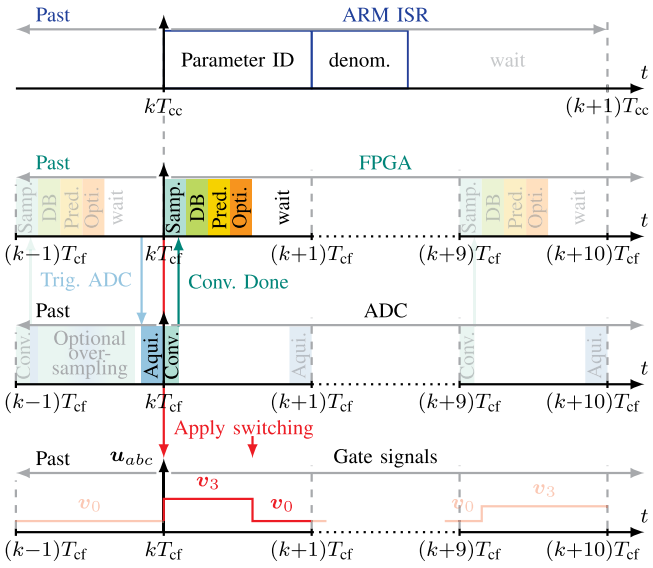

Fig. 10. Timing sequence of the proposed heterogeneous computing.

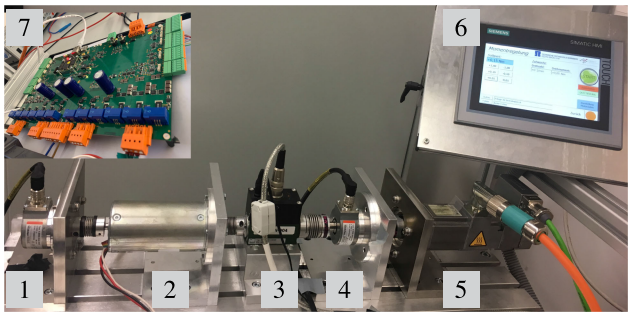

Fig. 11. Test bench: (1) motor speed encoder, (2) test motor (PMSM), (3) torque measuring shaft, (4) load speed encoder, (5) load machine, (6) HMI for the load machine, (7) SoC platform, combined with the VSI.

prediction would require, resource streaming is used. This allows both mapping tasks, i.e., (25a) and (25b), to be implemented only once, but they can be used in all prediction steps. However, even though linear interpolation is used for the maps in the FPGA, only 40 ns—using a 25 MHz clock—are required for each conversion. Therefore, the additional time through streaming is manageable. It should be noted that the flux linkage maps in the RAM, accessed by the processor, typically have a more precise granularity. Hence, more complex interpolation and extrapolation strategies than those implemented on the FPGA can be employed, as explained in Section IV-C. Nonetheless, as mentioned in that section, since each map exists in two copies, it is possible to avoid extrapolation for the FPGA implementation. This means that if, e.g., the measuring range of the current sensor is $[-30, 30]$ A, the processor uses IDW to calculate a flux linkage map that covers a range $[-32, 32]$ A with a step size of 1 A. The derived data are finally written to the FPGA at any update rate to improve the FPGA-implemented flux linkage maps.

Fig. 10 summarizes the interaction between the mentioned tasks and illustrates the timing behavior. Oversampling with a factor of eight is implemented for reading the ADCs, but

TABLE II
RESOURCE AND TIMING EVALUATION FOR $N_P = 2$

Resources	LUT as logic	LUT as memory	Block RAMs	Slice registers (flip-flops)	DSP slices
L-VSP^{2}CC	30983	1134	32	30310	119
ψ-VSP^{2}CC	39776	1470	37	36723	135
FOC	21652	1114	32	21675	52

Timing	Sampling & dq trans.	Deadbeat pre-selection	Prediction & VSP^{2}CC	Optimization & minimization	Total
L-VSP^{2}CC	1.6 µs	0.3 µs	0.9 µs	0.38 µs	3.18 µs
ψ-VSP^{2}CC	1.6 µs	0.3 µs	1.9 µs	0.38 µs	4.18 µs
FOC	1.6 µs	—	—	—	2.21 µs

TABLE III
MOTOR AND SYSTEM PARAMETERS IN THE LINEAR REGION

Description	Symbol	Motor M1 Bühler 1.25.058.401	Motor M3 ebm-papst ECI-63.20-K1-B00	Motor M4 Prototype
Rated torque	T_N	40 Ncm	36 Ncm	90 Ncm
Rated current	I_N	8.6 A	8.5 A	—
Rated speed	n_N	3000 rpm	3000 rpm	800 rpm
Winding resistance	R_{ph}	0.07 Ω	0.09 Ω	0.29 Ω
d-axis inductance	L_d	0.2 mH	0.14 mH	0.49 mH
q-axis inductance	L_q	0.2 mH	0.21 mH	2.10 mH
PM flux constant	ψ_{PM}	6.0 mVs	6.0 mVs	20 mVs
Pole pair number	p	4	4	4
dc-link voltage	V_{dc}	24 V	24 V	24 V
Sampl. & ctrl. freq.	f_{cf}	100 kHz	100 kHz	100 kHz

it is not required for the current sensors used, and it is thus inactive. The data acquisition is triggered immediately before a possible switching transition to avoid possible oscillations. The conversion and readout are subsequently performed.

For the subsequent comparison in Section VI, the two VSP^{2}CC approaches, i.e., L-VSP^{2}CC (inductance-based) and ψ-VSP^{2}CC (flux linkage-based), are evaluated on the proposed platform. For reasons of comparison, a conventional control solution, i.e., field-oriented control (FOC) with conventional SVM, is also implemented. A two-level VSI in combination with the Zynq-SoC is used for the implementation and experimental verification. The test bench is shown in Fig. 11.

B. Resource and Timing Evaluation

Table II shows the required total resources and the achieved timing when implementing the algorithm on an FPGA with a basic clock frequency of 100 MHz. The individual calculations are highlighted with the same colors as in Fig. 10. Even if the resources depend on the specific way of implementation (sharing and streaming), the provided information provides insight since it can indicate the required resources and/or computational load for an increased horizon and/or more complex cost functions. The fixed-point value range is chosen based on a normalized (p.u.) scaling. It should be mentioned that for the comparison of the two predictive approaches, apart from the prediction process itself [i.e., (5) as opposed to (7)], all intellectual property (IP) cores are identical and use the same clocks. This means that, e.g., the ADC readout, the cost function, and the deadbeat solution are completely identical.

The main difference between the two VSP^{2}CC approaches is the use of flux linkage maps in case of the ψ-based method.

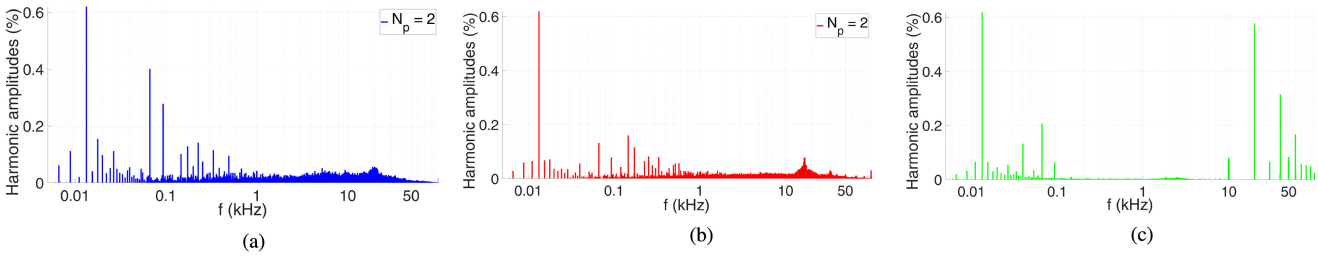

Fig. 12. Motor M3: Three-phase stator current spectrum at $i_d^*=-5.0$ A, i_q^*=18.03 A, and n_m=200 rpm (experimental results). (a) L-VSP^{2}CC: $f_\mathrm{sw}\approx 10.2$ kHz, $I_\mathrm{THD}=1.85\%$. (b) ψ-VSP^{2}CC: $f_\mathrm{sw}\approx 10.3$ kHz, $I_\mathrm{THD}=1.48\%$. (C) FOC: $f_\mathrm{sw}=10.0$kHz, $I_\mathrm{THD}=1.49\%$.

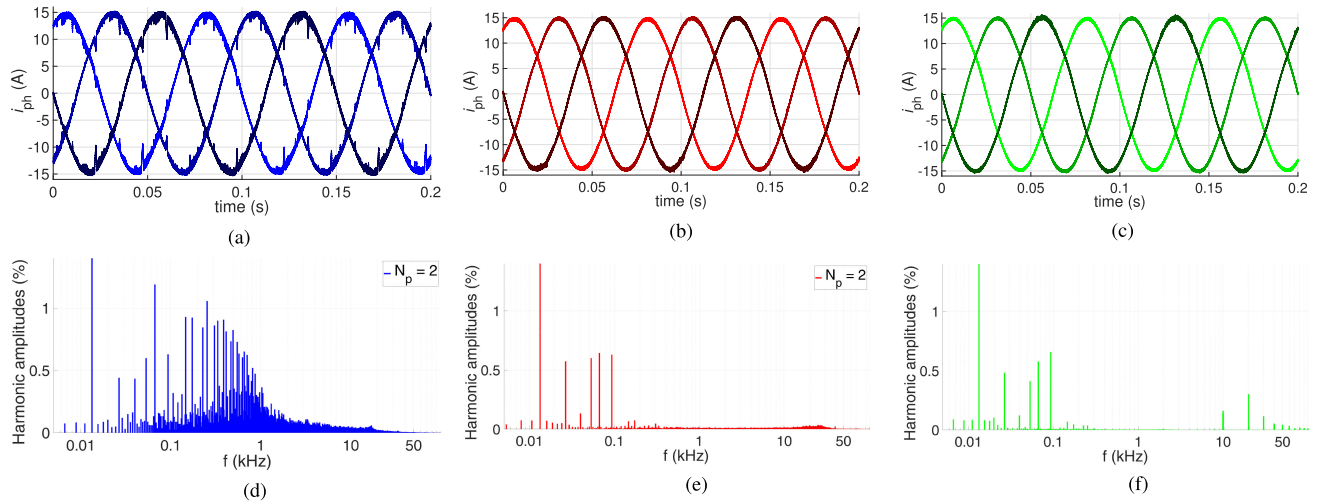

Fig. 13. Motor M4: Three-phase stator current and corresponding spectrum at $i_d^*=-5$ A, i_q^*=14 A and n_m=200 rpm (experimental results). (a) L-VSP^{2}CC: $f_\mathrm{sw}\approx 13.17$ kHz. (b) ψ-VSP^{2}CC: $f_\mathrm{sw}\approx 10.0$ kHz. (c) FOC: $f_\mathrm{sw}=10.0$ kHz. (d) L-VSP^{2}CC: $I_\mathrm{THD}=5.28\%$. (e) ψ-VSP^{2}CC: $I_\mathrm{THD}=1.90\%$. (f) FOC: $I_\mathrm{THD}=1.81\%$.

At this point, it is worth mentioning that flux linkage maps are preferred to polynomial solutions for reasons related to resource efficiency; see Section III. Specifically, for the bivariate extension, two terms (one for self- and one for cross-saturation) and, therefore, two multiplications, are required for each polynomial order. Moreover, a third term describes the impact of the permanent magnets. Thereby, it can be concluded that when comparing the calculation effort of both options and taking into account the subsequent FPGA implementation, the flux linkage maps constitute a computationally cheaper method. Finally, FOC requires only about half of the resources needed for the proposed direct MPC algorithm.

VI. Performance Evaluation

The good steady-state and dynamic behavior of the L-VSP^{2}CC was shown in [15]. Therein, low current distortions and fast transient responses for a PMSM-based drive system were presented. As shown in this section, such features remain in place with the proposed VSP^{2}CC scheme that utilizes flux linkage maps (i.e., ψ-VSP^{2}CC). Moreover, such a favorable performance is even more pronounced with nonlinear machines. To show this, one PMSM with (mostly) linear behavior, i.e., motor M1, and two nonlinear machines (M3 and M4) are used as case studies. The parameters of the systems under consideration are provided in Table III, while the flux linkage maps of motors M3 and M4 are shown in Fig. 5(a)–(b) and (c)–(d), respectively. Motors M1 and M3 are commercial ones, whereas motor M4 is a self-built prototype with tooth coil winding and a resulting fractional slot winding, making the spatial harmonics in the machine design more pronounced. Finally, FOC serves as a benchmark for comparing the performance of the proposed ψ-VSP^{2}CC as well as that of the L-VSP^{2}CC [15]. Note that for a fair and meaningful comparison, in all the examined cases that follow, the weighting factor λ_u in the DMPC methods is adjusted such that (approximately) the same average switching frequency f_sw results for operation under the same conditions.

A. Steady-State Performance—Stator Current

Figs. 12 and 13 present the steady-state performance of motors M3 and M4, respectively, with both VSP^{2}CC approaches and FOC. Fig. 13 shows the three-phase stator currents and corresponding harmonic spectra, whereas Fig. 12 focuses only on the harmonic distortions. The chosen operating point—as indicated by the current reference values—is in the range of

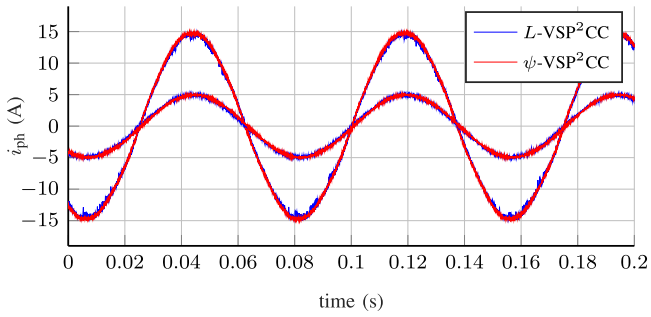

Fig. 14. Motor M4: Single-phase stator current at $i_d^*=-5.0$ A, i_q^*=14.0 A, n_{m}=200 rpm, $f_{\mathrm{sw}}\approx 16$ kHz, and N_{p}=2. For comparison, an operating point without saturation, i.e., i_d^*=0 A, i_q^*=5.0 A, is shown (experimental results).

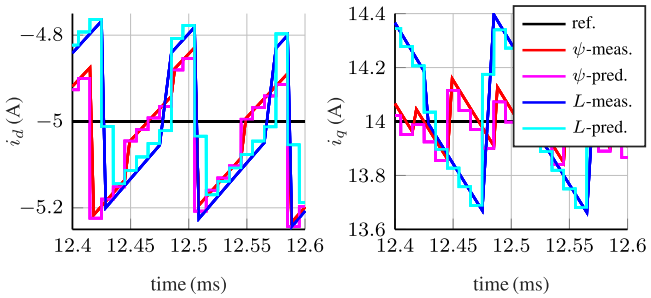

Fig. 15. Motor M3: VSP^{2}CC at $\angle\boldsymbol{\psi}_{dq}=30°$ with $f_{\mathrm{sw}}\approx 11.5$ kHz and $n_{\mathrm{m}}=$ 100 rpm (simulation results).

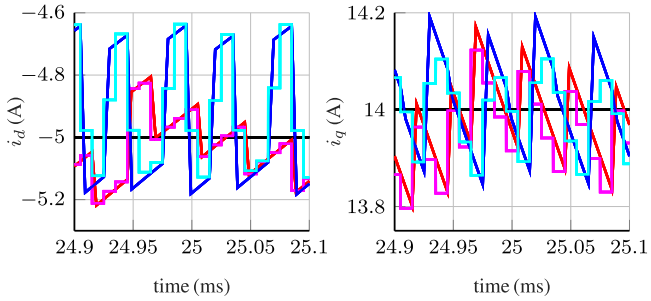

Fig. 16. Motor M3: VSP^{2}CC at $\angle\boldsymbol{\psi}_{dq}=60°$ with $f_{\mathrm{sw}}\approx 11.5$ kHz and $n_{\mathrm{m}}=$ 100 rpm (simulation results).

current saturation. Moreover, to clearly demonstrate the benefits of ψ-VSP^{2}CC, operation at low speed, i.e., low modulation index, is shown since parameter inaccuracies, e.g., inductance mismatches, have a stronger impact on the system performance in such operating conditions; see Fig. 8. As can be seen, when considering the current THD as a performance metric, ψ-VSP^{2}CC outperforms L-VSP^{2}CC, while it is similar to the conventional control solution, i.e., FOC with SVM. The improved steady-state performance is even more pronounced with the prototype motor M4 due to its stronger nonlinear magnetic behavior. Finally, it should be pointed out that due to the rather linear nature of motor M1, L-VSP^{2}CC and ψ-VSP^{2}CC—on the basis that the inductances are correctly identified—exhibit identical behavior (see the results in Fig. 8), and, thus, further analysis on this drive system is omitted hereafter.

The improved steady-state behavior is further demonstrated in Fig. 14, where the phase current for two different operating points is shown when using L- and ψ-VSP^{2}CC. Due to the saturation caused by an increasing reference current, the current ripple and THD of L-VSP^{2}CC also increases. At this point it is worth mentioning that the THD contains low- and high-order harmonics, see, e.g., the harmonic spectra in Fig. 13. The former are generally due to the geometry and winding concept of the machine, while the latter due to the switching behavior. As a result, besides the typical low-order harmonics, such as the fifth and seventh, the M4 prototype also exhibits the second and fourth harmonic due to the fractional slot winding. As explained in Section III, the flux linkage maps are identified by averaging over all rotor positions and several turns for memory and computational reasons. Thus, neither the flux linkage maps nor the inductances, i.e., neither of the discussed approaches, take into account the low-order harmonics.[14] However, despite the unmodeled spatial harmonics, i.e., the unaddressed low-order harmonics, the harmonics due to switching are significantly less with ψ-VSP^{2}CC as compared to those of L-VSP^{2}CC, while they are similar to those of FOC with SVM. This is also reflected in the current THD of the three methods.

For better understanding and deeper insight, Figs. 15 and 16 show the steady-state behavior of the i_d and i_q currents for the nonlinear motor M3. As can be seen, L-VSP^{2}CC leads to an unnecessarily high current ripple (see the measured current shown with the blue line) and—consequently—high THD due to the poor prediction of t_{z} (see the predicted current shown with the light blue line) resulting from a mismatch between the values of the prediction-model and real-world inductance. In contrast, the proposed ψ-VSP^{2}CC, which uses the flux linkage maps [see Figs. 5(a) and (b)] in the prediction, computes the VSP instant t_{z} so that the current ripple (red line) is significantly lower, even in the case of saturation. As a result, the current THD also reduces. Such a behavior is also experimentally verified, e.g., by comparing the current ripple of motor M4; see Fig. 17.

Based on the presented results, it can be observed that the current ripple is also affected by the position of the rotor flux vector within the triangular sectors formed by the voltage SVs. As mentioned in, e.g. [50], the current ripple is higher when the flux vector is located in the middle of each sector. This is the case regardless of the modulation/control method used since it depends on the relative position of the flux vector with respect to the voltage SVs. More specifically, the closer the flux is to the voltage SVs, the smaller the voltage difference between the induced and applied voltage, and, consequently, the smaller the current ripple. However, as can be seen in Figs. 15 and 16, there is a significant difference in the current prediction performed by the two VSP^{2}CC methods. For example, in the middle of the sector, e.g., at 30°, the current error on the q-axis is more dominant for L-VSP^{2}CC, whereas at the sector borders, e.g., at 60°, it is the other way around, i.e., the d-axis error is bigger. Considering the flux linkage maps in Figs. 5(a) and (b), it can be noticed that the

[14]To keep the computational effort low, while still considering the spatial harmonics, an alternative is to use a voltage correction term, similar, e.g., to [26, p. 25]

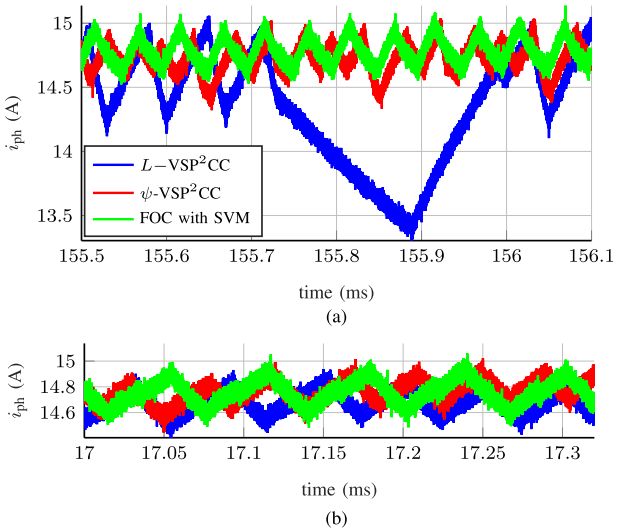

Fig. 17. Motor M4: Single-phase stator current ripple (a) for the operating point in Fig. 13 and (b) at n_m=800 rpm, for VSP^{2}CC with N_p=2 and FOC with SVM (experimental results). (a) $i_d^* = -5$ A, $i_q^* = 14$ A, $n_m = 200$ rpm, $f_{sw} \approx 10$ kHz. (b) $i_d^* = -5$ A, $i_q^* = 14$ A, $n_m = 800$ rpm, $f_{sw} \approx 16$ kHz.

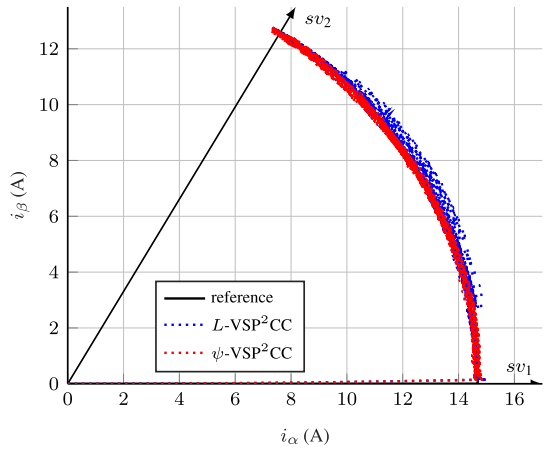

Fig. 18. Motor M3: Current for the first sector at $i_d^* = -5$ A, $i_q^* = 14$ A at steady state for VSP^{2}CC with N_p=2 at $n_m = 100$ rpm (simulation results).

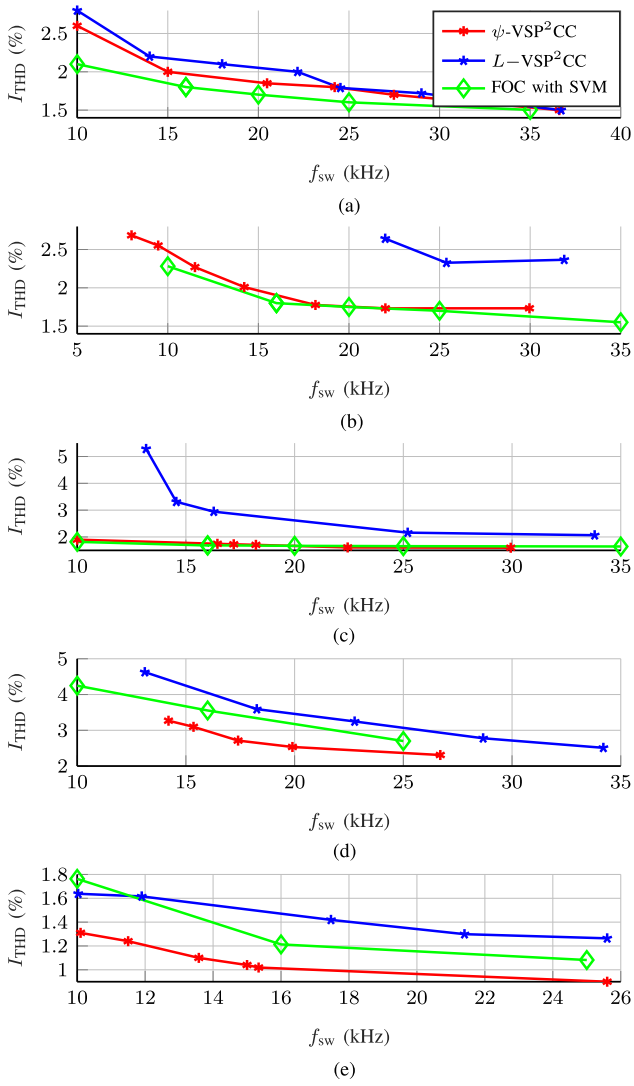

Fig. 19. Motor M4: Trade-off between I_{THD} and f_{sw} for VSP^{2}CC with N_p=2 and FOC with SVM (experimental results). (a) $i_d^* = 0$ A, $i_q^* = 5$ A, $n_m = 200$ rpm. (b) $i_d^* = 0$ A, $i_q^* = 15$ A, $n_m = 200$ rpm. (c) $i_d^* = -5$ A, $i_q^* = 14.0$ A, $n_m = 200$ rpm. (d) $i_q^* = 0$ A, $i_q^* = 5$ A, $n_m = 800$ rpm. (e) $i_d^* = -5$ A, $i_q^* = 14$ A, $n_m = 800$ rpm.

saturation effect on the q-axis is more pronounced than that on the d-axis. Since for the chosen case studies the q-component of the reference current prevails, i.e., $|i_q^*| > |i_d^*|$, when it is aligned with a voltage SV, then a suboptimal prediction has a stronger adverse effect on the system performance. As a result, L-VSP^{2}CC produces an even higher current ripple at the middle of each sector; see Fig. 18. On the other hand, as can be seen in the same figure, ψ-VSP^{2}CC successfully tackles this issue, thanks to the more accurate current prediction.

B. Steady-State Performance—Performance Trade-Off Curves

To further elucidate the potential performance benefits of the proposed MPC method, the steady-state performance trade-off curves between current THD (I_{THD}) and switching frequency (f_{sw}) are analyzed in Fig. 19 for the three different control approaches when using motor M4. The evaluation shows that the more heavily the control effort is penalized (i.e., the lower f_{sw} gets by increasing the value of λ_u), the more important the prediction model accuracy becomes. This means that at lower switching frequencies f_{sw}, the difference in current THD generated by L- and ψ-VSP^{2}CC becomes bigger.

It is also evident that a bigger voltage margin is required for operation at higher speeds, implying that VSP^{2}CC employs active voltage SVs more frequently than zero voltage SVs. As a result, the impact of a VSP-based MPC scheme is not that strong. On the other hand, for low-speed operation, where zero voltage SVs are mostly used and active SVs are only required for a shorter duration, the advantage of VSP^{2}CC is obvious, since a VSP can lead to low current ripple while achieving a low switching frequency (compared to conventional DMPC [4]). Even though this trend is, at first, independent of the VSP^{2}CC

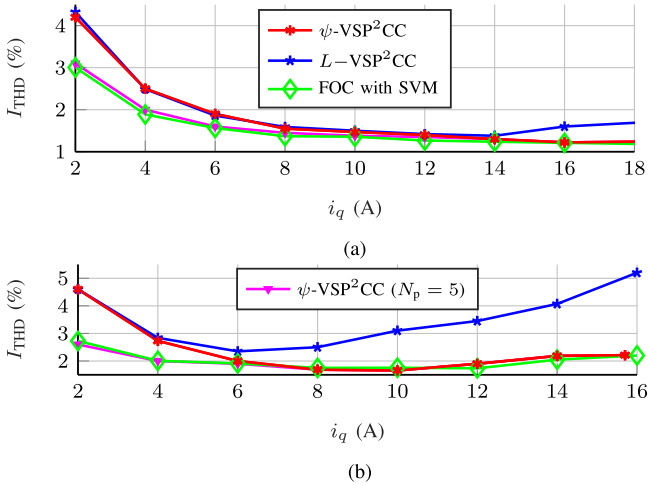

Fig. 20. Trade-off between I_{THD} and i_q for ψ- and L-VSP^{2}CC with N_p=2, ψ-VSP^{2}CC with N_p=5, and FOC with SVM (experimental results). (a) Motor M3: $i_d^*=0$ A, $f_\text{sw}\approx 16$ kHz, $n_\text{m}=200$ rpm. (b) Motor M4: $i_d^*=0$ A, $f_\text{sw}\approx 10$ kHz, $n_\text{m}=200$ rpm.

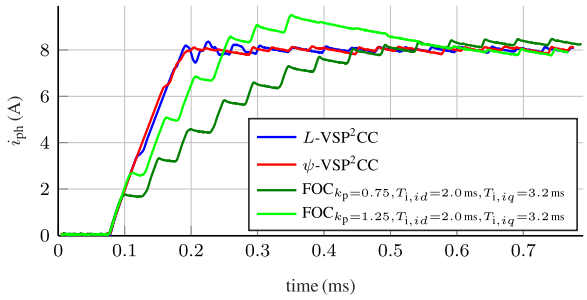

Fig. 21. Motor M3: Single-phase stator current during transient with $i_d^*=0$ A, $i_q^*=8$ A at $n_\text{m}=0$ rpm and $f_\text{sw}\approx 10$ kHz (experimental results).

method used, i.e., L-VSP^{2}CC [15] or ψ-VSP^{2}CC, once saturation and cross-coupling occur at higher values of the current reference, ψ-VSP^{2}CC can still compute VSPs that enable current ripple reduction. As a result, ψ-VSP^{2}CC shows the biggest performance improvement at lower speeds; see Fig. 19.

In addition, Fig. 20(a) shows that a visible difference between the two VSP^{2}CC approaches due to the nonlinear magnetic behavior starts at motor M3 in the range of the nominal current, i.e., $\sqrt{2}I_\text{N}=12.02$ A. For motor M4, such discrepancies in the current THD are even more pronounced and become evident at lower currents since saturation starts already at 4 A, as shown in Fig. 20(b). Furthermore, a longer prediction horizon, e.g., N_p=5, is required for operation at a very low modulation index, i.e., at very low currents and speeds, to achieve a comparable THD with FOC with SVM.

Given the presented results for the steady-state operation of the examined drive systems, it can be claimed that the proposed ψ-VSP^{2}CC method clearly outperforms the L-VSP^{2}CC discussed in [15]. The current distortions, as quantified by the current THD, significantly decrease, especially when machines with nonlinear magnetic behavior are of concern. Moreover, the proposed method achieves the same steady-state behavior as FOC with SVM. It is worth mentioning, however, that by further increasing the sampling/control frequency so as to increase the ratio between the sampling and switching frequencies, the switching granularity can be further improved. This will lead to an even better performance of ψ-VSP^{2}CC, as reported in [4, Section V].

C. Transient Performance

Besides the steady-state behavior, the transient behavior of the drive systems is of interest. Richter [26] and Kellner [35] showed that the dynamic behavior of nonlinear machines can be improved by compensating at least for the delay time independently of the control approach used. However, by accounting for the nonlinear model in the prediction and optimization processes, an even more significant improvement can be achieved.

This is demonstrated in Figs. 21 and 22, where, as it can be seen, VSP^{2}CC—regardless of the prediction method—provides faster current responses than FOC. Both VSP^{2}CC approaches have the freedom to initially use only active voltage SVs, whereas FOC with SVM has to implement zero SVs which detract from the transient response. To improve the transient performance of the latter, i.e., to reduce (avoid) the turn-on time of the zero SVs and thus to exploit the available voltage margin more effectively, it is common practice to change the SVM pattern depending on the operating point, e.g., alternating between continuous SVM at low speeds (i.e., at low modulation indices) and discontinuous SVM or switching with the fundamental frequency at high speeds (i.e., at high modulation indices). However, it is not straightforward how to define a suitable criterion based on which the SVM pulse pattern is chosen, although a hysteresis band can be implemented to avoid toggling [51]. Furthermore, even if the PI controllers in the inner loop of FOC were tuned according to the modulus optimum method such that a high bandwidth is achieved, the transient performance of FOC can be improved by tuning them more aggressively. This improvement, however, will be realized at the expense of current overshoots.

Comparing the VSP^{2}CC approaches, the improved gradient calculation achieved with ψ-VSP^{2}CC leads not only to an improved THD at steady state, but also to less oscillation during transients. When saturation is present, L-VSP^{2}CC calculates suboptimal switching points once the current reaches its reference, resulting in unnecessarily high current ripple—see Fig. 22(a)—and torque ripple; see Fig. 22(b). At higher speeds [see Fig. 22(c)], the voltage amplitude is bigger, so an accurate VSP is less important and the negative influence is smaller. Note that in Figs. 21 and 22, the d-axis is aligned with the a-phase at the beginning of the transient. Hence, the a-phase current initially rises, while b- and c-phase currents decrease.

Finally, the performance of the proposed and benchmark controllers are tested under changes in the speed. Specifically, Fig. 23 shows the phase currents and torque when the load machine changes the speed. As can be seen, all controllers exhibit good behavior, although the quality of the current and torque with ψ-VSP^{2}CC is clearly higher (i.e., less ripples), as also demonstrated in Section VI-A.

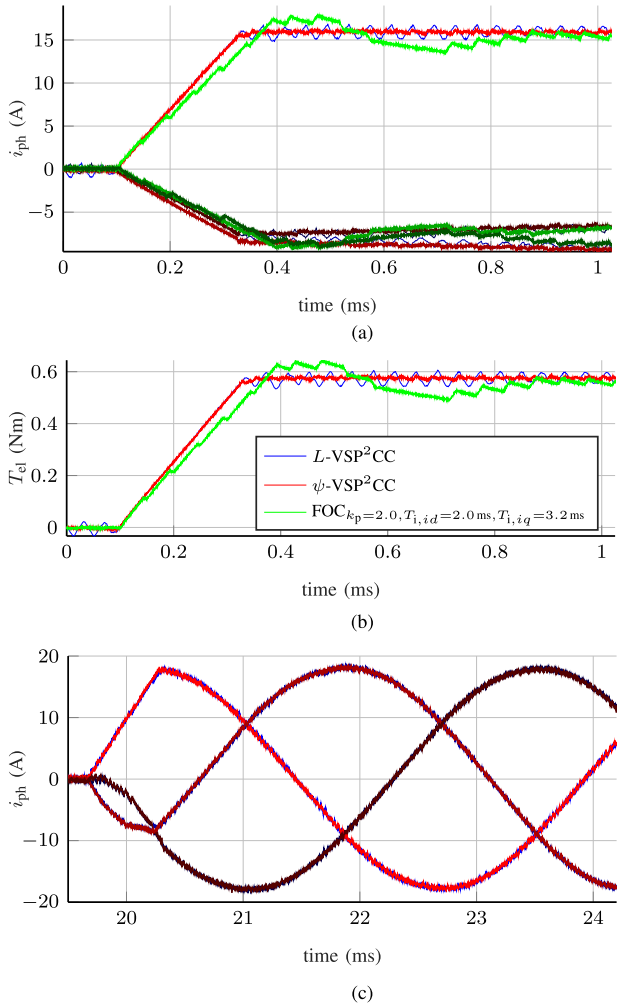

Fig. 22. Motor M3: Three-phase stator current and electromagnetic torque for L- and ψ-VSP^{2}CC and FOC during transient operation for an i_q^* step change when i_d^*=0 A, $f_{sw} \approx 20$ kHz, N_p=2. For clarity, the FOC currents are not shown in (c). The same color codes for the currents are used as in Fig. 13 (experimental results). (a) Step-change from i_q^*=0 A to i_q^*=16.0 A at n_m=200 rpm. (b) Electromagnetic torque for a step change from i_q^*=0 A to i_q^*=16.0 A. (c) Step-change from i_q^*=0 A to i_q^*=18.24 A at n_m=3000 rpm.

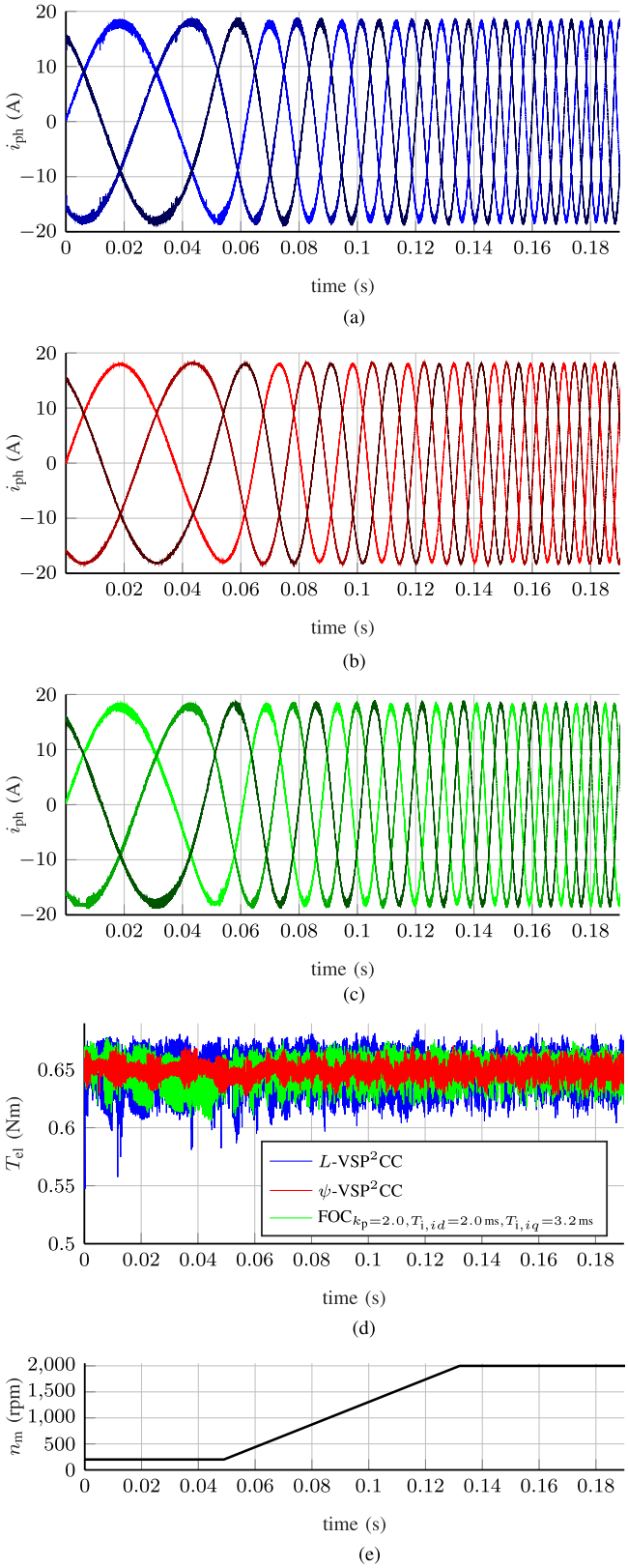

Fig. 23. Motor M3: Three-phase stator current during a load speed change from n_m=200 to 2000 rpm with i_q^*=18.03 A, i_d^*=0 A. $f_{sw} \approx 20.0$ kHz before the transient occurs and $N_p = 2$ (experimental results). (a) L-VSP^{2}CC with $\lambda_u = 0.09$. (b) ψ-VSP^{2}CC with $\lambda_u = 0.07$. (c) FOC with k_p=2.0, $T_{i,id}$ = 2.0 ms, $T_{i,iq}$ = 3.2 ms. (d) Electromagnetic torque during speed change. (e) Rotor shaft speed of the load machine.

D. Final Assessment

The combination of the two performance criteria for nonlinear IPMSMs, i.e., THD and transient response, shows the great advantage of the presented approach. More specifically, ψ-VSP^{2}CC can be executed at a frequency of 100 kHz, but it operates the drive system at a switching frequency much lower than that, depending on the operating point. This can be achieved by adjusting the weighting factor λ_u which determines the trade-off between the current distortions and the switching frequency. Such an ability to adapt the switching frequency depending on the operating point (e.g., at different motor speeds) is particularly advantageous for electric drives, as switching only takes place when required. As a result, unnecessary switching power losses can be avoided. FOC, on the other hand, makes decisions at a much lower frequency rate, which is double of the (constant) switching frequency, regardless of the operating

point. In addition, when using FOC, the PI gains must be adapted depending on the operating point.

The above imply that the proposed ψ-VSP^{2}CC shifts the control effort from the design to the computational stage. The latter, nevertheless, is simplified, thanks to the control platform used; see Section V. Finally, it is important to point out that by adopting even more powerful control platforms that are readily available [48], the performance of ψ-VSP^{2}CC can be further improved by increasing the control frequency and thus the granularity of switching [4].

VII. Conclusion

This article presented an extension of the VSP^{2}CC algorithm published in [15], which uses the flux linkage instead of the machine inductances for the stator current prediction. In doing so, the prediction accuracy, and thus the effectiveness of the implemented MPC algorithm, are tellingly enhanced when machines characterized by pronounced nonlinear phenomena, such as saturation and cross-coupling, are of concern, e.g., highly utilized IPMSMs. As a result, the drive performance, as quantified by the current distortions (i.e., current THD), is significantly improved. Such a favorable steady-state performance of the drive is also assisted by other inherent characteristic of VSP^{2}CC, most notably its high granularity stemming from the introduction of a VSP within the control interval. Moreover, thanks to the direct nature of the control scheme, very fast transients are achieved with very short settling times.

To support the aforementioned claims, simulation and experimental results demonstrated the potential benefits of the proposed method. As shown, the control algorithm in question clearly outperforms the VSP^{2}CC method, which bases its prediction on the machine inductances. Moreover, it achieves similar steady-state performance with FOC while exhibiting superior dynamic behavior. All thing considered, it can be stated that ψ-VSP^{2}CC is an interesting alternative to established control methods.

Finally, it is worth mentioning that, thanks to the versatility of the proposed method, its adaptation to other control tasks is possible. For example, the identified flux linkage maps can be used for maximum torque per ampere in base speed region and maximum torque per voltage in the field weakening region, as shown for nonlinear PMSM, e.g., in [52], [53]. However, if the use of the flux linkage leads to a significant increase in the computational load, thus making the real-time implementation of the proposed MPC algorithm challenging, an alternative approach is to use LUTs for the absolute inductances. In this way, (self-) saturation effects can be—to some extent—respected and the prediction error is—at least partially—minimized. Future work includes compensation for the rotor position dependency and iron loss effects to increase the prediction accuracy of VSP^{2}CC.

Appendix

A detailed derivation of the flux linkage change is provided hereafter. Using (6), the flux linkage change at time step $k+1$ is [19]

$$\psi_d(k+1) = \psi_d(k) + T_{\text{cf}}\Bigg(v_d(k) - R_{\text{ph}} i_d(k) + \frac{\omega_{\text{el}}}{2}\Bigg(\psi_q(k) \underbrace{+ \psi_q(k) + T_{\text{cf}}\Big(v_q(k) - R_{\text{ph}} i_q(k) - \frac{\omega_{\text{el}}}{2}\Sigma\psi_d(k+1)\Big)}_{\psi_q(k+1)}\Bigg)\Bigg) \tag{30a}$$

$$\psi_q(k+1) = \psi_q(k) + T_{\text{cf}}\Bigg(v_q(k) - R_{\text{ph}} i_q(k) - \frac{\omega_{\text{el}}}{2}\Bigg(\psi_d(k) \underbrace{+ \psi_d(k) + T_{\text{cf}}\Big(v_d(k) - R_{\text{ph}} i_d(k) + \frac{\omega_{\text{el}}}{2}\Sigma\psi_q(k+1)\Big)}_{\psi_d(k+1)}\Bigg)\Bigg). \tag{30b}$$

After rearranging and collecting terms, it yields

$$\psi_d(k+1) = \psi_d(k) + \frac{T_{\text{cf}}(v_d(k) - R_{\text{ph}} i_d(k) + \omega_{\text{el}}\psi_q(k))}{1 + \frac{1}{4}T_{\text{cf}}^2\omega_{\text{el}}^2} + \frac{T_{\text{cf}}^2\frac{\omega_{\text{el}}}{2}(v_q(k) - R_{\text{ph}} i_q(k) - \omega_{\text{el}}\psi_d(k))}{1 + \frac{1}{4}T_{\text{cf}}^2\omega_{\text{el}}^2} \tag{31a}$$

$$\psi_q(k+1) = \psi_q(k) + \frac{T_{\text{cf}}(v_q(k) - R_{\text{ph}} i_q(k) - \omega_{\text{el}}\psi_d(k))}{1 + \frac{1}{4}T_{\text{cf}}^2\omega_{\text{el}}^2} + \frac{T_{\text{cf}}^2\frac{\omega_{\text{el}}}{2}(-v_d(k) + R_{\text{ph}} i_d(k) - \omega_{\text{el}}\psi_q(k))}{1 + \frac{1}{4}T_{\text{cf}}^2\omega_{\text{el}}^2}. \tag{31b}$$

Further simplifications are valid. First, given that $T_{\text{cf}} \ll 1$, it holds that $\omega_{\text{el,max}} T_{\text{cf}} \ll 1$, where $\omega_{\text{el,max}}$ is the maximum electrical speed. In light of this, the last term of (31a) and (31b) can be neglected. Second, the denominator of the first term can be assumed to be constant and equal to one, since $\omega_{\text{el,max}}^2 T_{\text{cf}}^2 \approx 0$. However, since the formula should be valid in general, only the first assumption is implemented, whereas the second is not. Due to extreme conditions such as high speed drives at low sampling and control frequencies (e.g., $\omega_{\text{el}} = 1000\,\text{rps}$ and $T_{\text{cf}} = 1\,\text{ms}$), the aforementioned denominator can be greater than one. For this reason, the denominator is calculated on the processor and is kept constant for one complete prediction process, since the mechanical angular velocity can be assumed to be constant during the prediction process of the electrical model. With the above manipulations, assumptions, and simplifications, (7) results.

References

[1] C. Bordons and C. Montero, "Basic principles of MPC for power converters: Bridging the gap between theory and practice," *IEEE Ind. Electron. Mag*, vol. 9, no. 3, pp. 31–43, Sep. 2015.

[2] T. Geyer, P. Karamanakos, and R. Kennel, "On the benefit of long-horizon direct model predictive control for drives with LC filters," in *Proc. IEEE Energy Convers. Congr. Expo.*, Pittsburgh, PA, Sep. 2014, pp. 3520–3527.

[3] S. Wendel, A. Dietz, and R. Kennel, "FPGA based finite-set model predictive current control for small PMSM drives with efficient resource streaming," in *Proc. IEEE Int. Symp. Pred. Control Elect. Drives Power Electron.*, Pilsen, Czech Republic, Sep. 2017, pp. 66–71.

[4] P. Karamanakos and T. Geyer, "Guidelines for the design of finite control set model predictive controllers," *IEEE Trans. Power Electron.*, vol. 35, no. 7, pp. 7434–7450, Jul. 2020.

[5] P. Landsmann and R. Kennel, "Saliency-based sensorless predictive torque control with reduced torque ripple," *IEEE Trans. Power Electron.*, vol. 27, no. 10, pp. 4311–4320, Oct. 2012.

[6] P. Karamanakos, P. Stolze, R. M. Kennel, S. Manias, and H. du T. Mouton, "Variable switching point predictive torque control of induction machines," *IEEE J. Emerg. Sel. Topics Power Electron.*, vol. 2, no. 2, pp. 285–295, Jun. 2014.

[7] P. Stolze, P. Karamanakos, M. Tomlinson, R. Kennel, T. Mouton, and S. Manias, "Heuristic variable switching point predictive current control for the three-level neutral point clamped inverter," in *Proc. IEEE Int. Symp. Pred. Control Elect. Drives Power Electron.*, Munich, Germany, Oct. 2013, pp. 1–8.

[8] L. Tarisciotti, P. Zanchetta, A. Watson, J. C. Clare, M. Degano, and S. Bifaretti, "Modulated model predictive control for a three-phase active rectifier," *IEEE Trans. Ind. Appl.*, vol. 51, no. 2, pp. 1610–1620, Mar./Apr. 2015.

[9] Y. Zhang, W. Xie, Z. Li, and Y. Zhang, "Low-complexity model predictive power control: Double-vector-based approach," *IEEE Trans. Ind. Electron.*, vol. 61, no. 11, pp. 5871–5880, Nov. 2014.

[10] Y. Zhang, D. Xu, J. Liu, S. Gao, and W. Xu, "Performance improvement of model-predictive current control of permanent magnet synchronous motor drives," *IEEE Trans. Ind. Appl.*, vol. 53, no. 4, pp. 3683–3695, Jul.–Aug. 2014.

[11] Y. Zhang, Y. Peng, and H. Yang, "Performance improvement of two-vectors-based model predictive control of PWM rectifier," *IEEE Trans. Power Electron.*, vol. 31, no. 8, pp. 6016–6030, Aug. 2016.

[12] L. Tarisciotti *et al.*, "Model predictive control for shunt active filters with fixed switching frequency," *IEEE Trans. Ind. Appl.*, vol. 53, no. 1, pp. 296–304, Jan.–Feb. 2017.

[13] Y. Zhang, Y. Bai, and H. Yang, "A universal multiple-vector-based model predictive control of induction motor drives," *IEEE Trans. Power Electron.*, vol. 33, no. 8, pp. 6957–6969, Aug. 2018.

[14] P. Karamanakos, R. Mattila, and T. Geyer, "Fixed switching frequency direct model predictive control based on output current gradients," in *Proc. IEEE Ind. Electron. Conf.*, Washington, DC, Oct. 2018, pp. 2329–2334.

[15] S. Wendel, P. Karamanakos, A. Dietz, and R. Kennel, "Operating point dependent variable switching point predictive current control for PMSM drives," in *Proc. IEEE Int. Symp. Pred. Control Elect. Drives Power Electron.*, Quanzhou, China, May/Jun. 2019, pp. 1–6.

[16] A. Mora, R. Cárdenas-Dobson, R. P. Aguilera, A. Angulo, F. Donoso, and J. Rodríguez, "Computationally efficient cascaded optimal switching sequence MPC for grid-connected three-level NPC converters," *IEEE Trans. Power Electron.*, vol. 34, no. 12, pp. 12464–12475, Dec. 2019.

[17] C. Zheng, T. Dragičević, B. Majmunović, and F. Blaabjerg, "Constrained modulated-model predictive control of an LC-filtered voltage source converter," *IEEE Trans. Power Electron.*, vol. 35, no. 2, pp. 1967–1977, Feb. 2020.

[18] P. Karamanakos, M. Nahalparvari, and T. Geyer, "Fixed switching frequency direct model predictive control with continuous and discontinuous modulation for grid-tied converters with LCL filters," *IEEE Trans. Control Syst. Technol.*, in press, doi: 10.1109/TCST.2020.3008030.

[19] J. Richter and M. Doppelbauer, "Predictive trajectory control of permanent-magnet synchronous machines with nonlinear magnetics," *IEEE Trans. Ind. Electron.*, vol. 63, no. 6, pp. 3915–3924, Jun. 2016.

[20] B. Štumberger, G. Štumberger, D. Dolinar, A. Hamler, and M. Trlep, "Evaluation of saturation and cross-magnetization effects in interior permanent-magnet synchronous motor," *IEEE Trans. Ind. Appl.*, vol. 39, no. 5, pp. 1264–1271, Sep.–Oct. 2003.

[21] M. Siami, D. A. Khaburi and J. Rodríguez, "Torque ripple reduction of predictive torque control for PMSM drives with parameter mismatch," *IEEE Trans. Power Electron.*, vol. 32, no. 9, pp. 7160–7168, Sep. 2017.

[22] X. Liu, L. Zhou, J. Wang, X. Gao, Z. Li, and Z. Zhang, "Robust predictive current control of permanent-magnet synchronous motors with newly designed cost function," *IEEE Trans. Power Electron.*, vol. 35, no. 10, pp. 10778–10788, Oct. 2020.

[23] X. Zhang, L. Zhang and Y. Zhang, "Model predictive current control for PMSM drives with parameter robustness improvement," *IEEE Trans. Power Electron.*, vol. 34, no. 2, pp. 1645–1657, Feb. 2019.

[24] P. G. Carlet, F. Tinazzi, S. Bolognani and M. Zigliotto, "An effective model-free predictive current control for synchronous reluctance motor drives," *IEEE Trans. Ind. Appl.*, vol. 55, no. 4, pp. 3781–3790, Jul.–Aug. 2019.

[25] X. Yuan, S. Zhang and C. Zhang, "Nonparametric predictive current control for PMSM," *IEEE Trans. Power Electron.*, vol. 35, no. 9, pp. 9332–9341, Sep. 2020.

[26] J. Richter, "Modellbildung, parameteridentifikation und regelung hoch ausgenutzter synchronmaschinen," Ph.D. dissertation, Fakultät für Elektrotechnik und Informationstechnik, Karlsruhe Institute of Technology, Karlsruhe, Germany, 2016.

[27] G. Weidenholzer, S. Silber, G. Jungmayr, G. Bramerdorfer, H. Grabner, and W. Amrhein, "A flux-based PMSM motor model using RBF interpolation for time-stepping simulations," in *Proc. Int. Elect. Mach. Drives Conf.*, Chicago, IL, USA, May 2013, pp. 1418–1423.

[28] A. Imura, T. Takahashi, M. Fujitsuna, T. Zanma, and S. Doki, "Dead-time compensation in model predictive instantaneous-current control," in *Proc. 38th Annu. Conf. IEEE Ind. Elect. Society*, Montreal, QC, Canada, Oct. 2012, pp. 5037–5042.

[29] S. Kuehl, P. Landsmann, and R. Kennel, "Bivariate polynomial approximation of cross-saturated flux curves in synchronous machine models," *in Proc. IEEE Int. Energy Conf. and Exhib.*, Florence, Italy, Sep. 2012, pp. 219–224.

[30] S. J. Underwood and I. Husain, "Online parameter estimation and adaptive control of permanent-magnet synchronous machines," *IEEE Trans. Ind. Electron.*, vol. 57, no. 7, pp. 2435–2443, Nov. 2009.

[31] J. Germishuizen and R. Tanner, "Stepped versus fixed rotor position FEA solutions for 2D flux linkage maps in machine design," in *Proc. Int. Conf. on Elect. Mach.*, Alexandroupoli, Greece, Sep. 2018, pp. 982–987.

[32] O. Wallscheid, T. Huber, W. Peters, and J. Böcker, "Real-time capable methods to determine the magnet temperature of permanent magnet synchronous motors-a review," in *Proc. 40th Annu. Conf. IEEE Ind. Elect. Soc.*, Dallas, TX, USA, Oct.–Nov. 2014, pp. 811–818.

[33] D. D. Reigosa, D. Fernandez, T. Tanimoto, T. Kato, and F. Briz, "Permanent-magnet temperature distribution estimation in permanent-magnet synchronous machines using back electromotive force harmonics," *IEEE Trans. Ind. Appl.*, vol. 52, no. 4, pp. 3093–3103, Jul.–Aug. 2016.

[34] W. Kirchgässner, O. Wallscheid, and J. Böcker, "Estimating electric motor temperatures with deep residual machine learning," *IEEE Trans. Power Electron.*, vol. 36, no. 7, pp. 7480–7488, Jul. 2021.

[35] S. Kellner, "Parameteridentifikation bei permanenterregten synchronmaschinen," Ph.D. dissertation, Technischen Fakultät, Universiät Erlangen-Nürnberg, Erlangen, Germany, 2012.

[36] X. Emery, "Simple and ordinary multigaussian kriging for estimating recoverable reserves," *Math. Geol.*, vol. 37, no. 3, pp. 295–319, Apr. 2005.

[37] J. B. Kim, K. Y. Hwang, and B. I. Kwon,"Optimization of two-phase in-wheel IPMSM for wide speed range by using the kriging model based on Latin hypercube sampling," *IEEE Trans. Magn.*, vol. 47, no. 5, pp. 1078–1081, May 2011.

[38] D. F. Watson and G. M. Philip "Triangle based interpolation," *J. Int. Assoc. Math. Geol.*, vol. 16, no. 8, pp. 779–795, Nov. 1984.

[39] G. Achilleos, "The inverse distance weighted interpolation method and error propagation mechanism - creating a DEM from an analogue topographical map," *J. Spatial Sci.*, vol. 56, no. 2, pp. 283–304, Dec. 2011.

[40] J. Richter, T. Gemaβmer, and A. Dollinger, "Iron loss and parameter measurement of permanent magnet synchronous machines," in *Proc. Int. Conf. on Elect. Mach.*, Berlin, Germany, Sep. 2014, pp. 1635–1641.

[41] S. L. Kellner, M. Seilmeier, and B. Piepenbreier, "Impact of iron losses on parameter identification of permanent magnet synchronous machines," in *Proc. Int. Elect. Drives Prod. Conf.*, Nuremberg, Germany, Sep. 2011, pp. 11–16.

[42] F. Bertele, U. Ammann, C. Cheshire, M. Neuburger, S. Piriienko, and T. Roesser, "Interpretation of measurement IPMSM flux tables for parameter identification," in *Proc. Eur. Power Electron. Conf.*, Genova, Italy, Sep. 2019, pp. 1–10.

[43] P. Karamanakos, A. Ayad, and R. Kennel, "A variable switching point predictive current control strategy for quasi-z-source inverters," *IEEE Trans. Ind. Appl.*, vol. 54, no. 2, pp. 1469–1480, Apr. 2018.

[44] I. Alevras, P. Karamanakos, S. Manias, and R. Kennel, "Variable switching point predictive torque control with extended prediction horizon," in *Proc. IEEE Int. Conf. Ind. Technol.*, Mar. 2015, pp. 2352–2357.

[45] P. Karamanakos, T. Geyer, and R. Kennel, "On the choice of norm in finite control set model predictive control," *IEEE Trans. Power Electron.*, vol. 33, no. 8, pp. 7105–7117, Aug. 2018.
[46] J. B. Rawlings and D. Q. Mayne, *Model Predictive Control: Theory and Design*. Madison, WI, USA: Nob Hill, 2009.
[47] L. Ortombina, P. Karamanakos and M. Zigliotto, "Robustness analysis of long-horizon direct model predictive control: Permanent magnet synchronous motor drives," in *Proc. 21st Workshop Control Model. Power Electron.*, Aalborg, Denmark, Nov. 2020, pp. 1–8.
[48] S. Wendel *et al.*, "UltraZohm-A powerful real-time computation platform for MPC and multi-level inverters," in *Proc. IEEE Int. Symp. Pred. Control of Elect. Drives Power Electron.*, Quanzhou, China, May–Jun. 2019, pp. 1–6.
[49] M. Dorfling, H. du T. Mouton, T. Geyer, and P. Karamanakos, "Long-horizon finite-control-set model predictive control with non-recursive sphere decoding on an FPGA," *IEEE Trans. Power Electron.*, vol. 35, no. 7, pp. 7520–7531, Jul. 2020.
[50] J. Holtz and B. Beyer, "Optimal pulsewidth modulation for ac servos and low-cost industrial drives," *IEEE Trans. Ind. Appl.*, vol. 30, no. 4, pp. 1039–1047, Jul.–Aug. 1994.
[51] A. M. Hava and R. J. Kerkman and T. A. Lipo, "A high-performance generalized discontinuous PWM algorithm," *IEEE Trans. Ind. Appl.*, vol. 34, no. 5, pp. 1059–1071, Sep.–Oct. 1998.
[52] Q. K. Nguyen, M. Petrich and J. Roth-Stielow, "Implementation of the MTPA and MTPV control with online parameter identification for a high speed IPMSM used as traction drive," *in Proc. Int. Power Electron. Conf.*, Hiroshima, Japan, May 2014, pp. 318–323.
[53] J. Bonifacio and R. Kennel, "On considering saturation and cross-coupling effects for copper loss minimization on highly anisotropic synchronous machines," *IEEE Trans. Ind. Appl.*, vol. 54, no. 5, pp. 4177–4185, Oct. 2018.

Sebastian Wendel (Student Member, IEEE) received the apprenticeship as an Electronics Technician from Koenig & Bauer AG, Germany, in 2009. He received, as part of a dual study program, the B.Eng. degree in electrical engineering and information technology and the M.Sc. degree in electronic and mechatronic systems from the Technische Hochschule Nürnberg, Nuremberg, Germany, in 2014 and 2016, respectively. He is currently working toward the Dr.-Ing. degree at the Technical University of Munich, Munich, Germany, in the field of model predictive control.

In 2015, he was as an Intern with the Digital Factory R&D, Siemens AG, Erlangen, Germany. From 2016 to 2020, he was a Research Assistant in the field of electrical drives with ELSYS, Technische Hochschule Nürnberg. In 2017, he was a Visiting Ph.D. Student at the Universidad de Santiago de Chile, Santiago de Chile, Chile. He is Co-Founder of the Zohm Control GmbH, Germany. His research interests include model predictive control, optimized control concepts, parameter identification, and the efficient implementation of control algorithms on heterogeneous SoC FPGAs.

Petros Karamanakos (Senior Member, IEEE) received the Diploma and Ph.D. degrees in electrical and computer engineering from the National Technical University of Athens (NTUA), Athens, Greece, in 2007 and 2013, respectively.

From 2010 to 2011, he was with the ABB Corporate Research Center, Baden-Dättwil, Switzerland. From 2013 to 2016, he was a PostDoc Research Associate with the Chair of Electrical Drive Systems and Power Electronics, Technical University of Munich, Munich, Germany. Since September 2016, he has been an Assistant Professor with the Faculty of Information Technology and Communication Sciences, Tampere University, Tampere, Finland. His research interests include the intersection of optimal control, mathematical programming, and power electronics, including model predictive control for power electronic converters and ac variable speed drives.

Dr. Karamanakos has received the 2014 Third Best Paper Award of the IEEE TRANSACTIONS ON INDUSTRY APPLICATIONS and two Prize Paper Awards at conferences. He serves as an Associate Editor of the IEEE TRANSACTIONS ON INDUSTRY APPLICATIONS and of the *IEEE Open Journal of Industry Applications*.

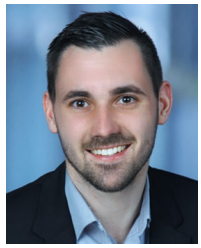

Philipp Gebhardt received the B.Eng. degree in mechanical engineering and the M.Sc. degree in electronic and mechatronic systems from the Technische Hochschule Nürnberg, Nuremberg, Germany, in 2018 and 2020, respectively.

From 2010 to 2018, he was an Intern with Robert Bosch GmbH, Nuremberg, Germany and Bosch Engineering GmbH, Holzkirchen, Germany. From 2018 to 2019, he was with ELSYS, Technische Hochschule Nürnberg. Since 2019, he has been an Application Engineer with Baumüller Nürnberg GmbH, Nuremberg, Germany. His research interests include control strategies and parameter identification for permanent magnet synchronous machines and their hydraulic applications.

Armin Dietz received the Dipl.-Ing. in electrical engineering from the Technical University of Munich, Munich, Germany, in 1988. He received the Dr.-Ing. degree from the Technical University of Munich, in 2003.

From 1988 to 2006, he was with Siemens AG, Erlangen, Germany, in different R&D and management positions; most recently he was R&D Manager for the business division "Actuators." Since 2006, he has been Professor with the Technische Hochschule Nürnberg, Nuremberg, Germany, where he has been, since 2008, the head of the Institute for Power Electronic Systems (ELSYS).

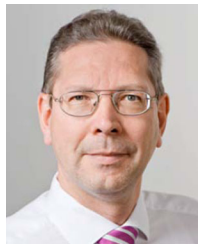

Ralph Kennel (Senior Member, IEEE) received the Dipl.-Ing. and Dr.-Ing. (Ph.D.) degrees from the University of Kaiserslautern, Kaiserslautern, Germany, in 1979 and 1984, respectively.

From 1983 to 1999, he worked on several positions with Robert Bosch GmbH, Germany. From 1994 to 1999, he was a Visiting Professor with the Newcastle University, Newcastle-upon-Tyne, U.K. From 1999 to 2008, he was Professor of Electrical Machines and Drives with Wuppertal University, Wuppertal, Germany. Since 2008, he is Professor of Electrical Drive Systems and Power Electronics with the Technical University of Munich, Munich, Germany. He was Extraordinary Professor with the University of Stellenbosch, South Africa, from 2016 to 2019, and a Visiting Professor with the Haixi Institute, Chinese Academy of Sciences, China, from 2016 to 2021. His research interests include today sensorless control of ac drives, predictive control of power electronics, and hardware-in-the-loop systems.

Dr. Kennel is a fellow of IET (former IEE) and a Chartered Engineer in the U.K. Within IEEE, he is Treasurer of the Germany Section as well as Distinguished Lecturer of the Power Electronics Society (IEEE-PELS). He has received the Harry Owen Distinguished Service Award from IEEE-PELS, in 2013, the EPE Association Distinguished Service Award, in 2015, and the 2019 EPE Outstanding Achievement Award. In 2018, he received the Doctoral degree honoris causa from Universitatea Stefan cel Mare in Suceava (Romania).